FACULDADE DE ENGENHARIA DA UNIVERSIDADE DO PORTO

FEUP

Radio-Frequency Transmitter for Subcutaneous Biomedical Implants

by

Américo Filipe dos Santos Dias

A thesis submitted in partial fulfillment of the requirements for the degree of
Master in Electrical and Computers Engineering
Telecommunications Major

Main advisor: **Pedro Guedes de Oliveira** (Ph.D.)

Co-advisor: **Cândido Duarte** (Eng.)

June 2010

(R114 D)

Copyright ©2010 by Américo Dias
americo.dias@fe.up.pt
Some Rights Reserved

This work is licensed under the terms of the *Creative Commons Attribution – Noncommercial – No Derivative Works 3.0* license available at http://creativecommons.org/licenses/by-nc-nd/3.0/

Attribution – Noncommercial – No Derivative Works

You are free:

To Share – to copy, distribute and transmit the work

Under the following conditions:

Attribution – You must attribute the work in the manner specified by the author or licensor (but not in any way that suggests that they endorse you or your use of the work).

Noncommercial – You may not use this work for commercial purposes.

No Derivative Works – You may not alter, transform, or build upon this work.

With the understanding that:

Waiver – Any of the above conditions can be waived if you get permission from the copyright holder.

Other Rights – In no way are any of the following rights affected by the license:

- Your fair dealing or fair use rights;
- The author's moral rights;
- Rights other persons may have either in the work itself or in how the work is used, such as publicity or privacy rights.

Notice – For any reuse or distribution, you must make clear to others the license terms of this work. The best way to do this is with a link to the web page http://creativecommons.org/licenses/by-nc-nd/3.0/.

Abstract

Biomedical engineering is one of the main trends for the future of technology as we know it. Intelligent biomedical implants are now a reality due to the large developments made in several engineering branches and medicine during the 20^{th} century.

The goal of this work is to develop a radio frequency transmitter for biomedical implants using the impulse-radio ultra-wideband technology. One of the possible applications for this transmitter is the biphasic Integrate-and-Fire system developed in the University of Florida. It consists on a neuronal recording system for brain-machine interfaces based on asynchronous biphasic-pulse coding. Other applications may be for example, cochlear implants, visual implants, among many others.

The Federal Communications Commission approved ultra-wideband in 2002 in the frequency bands between 0 to 960-MHz and 3.1 to 10.6-GHz. It presents itself as a good alternative to conventional narrowband transmitters in biomedical implants due to several factors like high bit-rate, low power consumption and simplicity of implementation since the complexity is passed to the receiver side.

This document presents the entire development process of the UWB transmitter, beginning with the analysis of existing implementations. The studied circuits were then compared and taken into account for the proposed architecture. When comparing to other known implementations found in literature, the presented work distinguishes itself for the higher bit-rate (1-Gbps) and for being one of the best solutions in terms of power consumption per pulse. Moreover, since high-frequency circuits are highly sensitive to several variations in terms of process and operation, the present solution also provides the ability for post manufacture tuning. Additionally, the present solution also offers a flexible modulation selection without compromising performance. Any IR-UWB modulation can be chosen by changing the driving scheme.

Two different 90-nm CMOS technologies were analyzed and simulations were performed in order to select the most appropriated. Physical implementation (layout) has been carried out using Cadence Virtuoso software. Design rule check, layout-versus-schematic and parasitic extraction were done using Mentor Graphics Calibre. To ensure the circuit functionality after the manufacturing process, process corner analysis of the post-layout netlist were also performed and calibration was tested for validation purposes. The transmitted pulses comply with the FCC spectrum mask and the total circuit occupies an area of 675x675-μm^2.

Resumo

A engenharia biomédica é uma das principais tendências para o futuro da tecnologia como a conhecemos. Implantes biomédicos inteligentes são hoje uma realidade, devido aos grandes desenvolvimentos feitos em vários ramos da engenharia e medicina, durante o século 20.

O objectivo deste trabalho é desenvolver um transmissor de rádio-frequência para implantes biomédicos usando a tecnologia *impulse-radio ultra-wideband*. Uma das aplicações possíveis para este transmissor é o sistema *Integrate-and-Fire*, desenvolvido na Universidade da Flórida. Este sistema consiste num circuito de leitura de sinais neuronais para interfaces cérebro-máquina baseado numa codificação bifásica assincrona. Outras aplicações possíveis podem ser, por exemplo, implantes cocleares, visuais, entre outros.

A tecnologia *ultra-wideband*, foi aprovada pela *Federal Communications Commission*, em 2002, nas bandas de frequência entre 0 e 960-MHz e entre 3,1 a 10,6-GHz. Apresenta-se como uma boa alternativa para os convencionais transmissores *narrowband* em implantes biomédicos devido a vários factores como maior velocidade na transferência de dados, baixo consumo de energia e a simplicidade de implementação uma vez que a complexidade é transferida para o receptor.

Este documento apresenta o processo de desenvolvimento do transmissor UWB, que se iniciou com uma análise das implementações existentes. Os circuitos estudados foram comparados e tidos em conta no processo de desenvolvimento da arquitectura proposta. O trabalho apresentado, destaca-se das implementações conhecidas pelo maior *bit-rate* (1-Gbps) e por ser uma das implementações com menor consumo de energia. Para além disso e uma vez que os circuitos de alta-frequência são altamente susceptíveis a variações do processo de fabrico, a presente arquitectura possui ainda mecanismos de ajuste que permitem a afinação após o fabrico. Esta solução permite ainda a implementação de qualquer modulação *impulse-radio ultra-wideband*.

Duas tecnologias CMOS de 90-nm foram analisadas e foram realizadas simulações com o intuito de seleccionar a mais indicada. A implementação física (*layout*) foi realizada utilizando o *software* Cadence Virtuoso. A verificação das regras de desenho, *layout-versus-schematic* e extracção de componentes parasitas foram realizadas utilizando o Mentor Graphics Calibre. Para garantir a funcionalidade do circuito mesmo com as variações de processo devido ao fabrico, foram realizadas simulações com variações extremas destes parâmetros (*corner analysis*). Os impulsos gerados cumprem o espectro aprovado pela FCC e a área total do circuito é 675x675-μm^2.

In memory of my father.

Acknowledgments

To my mother, who never lost the strength in the most difficult hours. To my sister for putting up with me for so many years...

To my girlfriend for her (almost) endless comprehension.

To my friend and co-advisor Cândido Duarte. Without his support, this thesis would certainly not have been written.

To my advisor Dr. Pedro Guedes de Oliveira and to Dr. Vitor Grade Tavares for their support and for believing in my work.

To all my friends from the Microelectronics Students' Group, specially to Daniel that helped me with the CAD software configuration.

To Alexander Singh, from the Computational NeuroEngineering Laboratory of the University of Florida, for his kindness in providing the neuronal signals used in figure 1.3.

And last but not least, to Malheiro and Amilcar, my fellows during the writing of this thesis. I wish them every success for their professional life.

"The science of today is the technology of tomorrow."

Edward Teller

Contents

Abstract i

Resumo iii

Acknowledgments vii

1 Introduction 1
- 1.1 Motivation . . . 1
  - 1.1.1 Integrate-and-fire system . . . 3
- 1.2 Objectives and proposed solution . . . 4
- 1.3 Document organization . . . 5

2 Background 7
- 2.1 Spectrum Regulations for Medical Use . . . 7
- 2.2 Narrowband transmitters . . . 7
- 2.3 Ultra-wideband transmitters . . . 9
  - 2.3.1 The Gaussian monocycle impulse . . . 10
  - 2.3.2 Direct sequence spread spectrum . . . 12
  - 2.3.3 Multi-band orthogonal frequency division multiplexing . . . 13
  - 2.3.4 Impulse-radio . . . 14
- 2.4 Ultra-wideband versus narrowband transmitters . . . 15

3 State of the art 17
- 3.1 Delay based impulse generator . . . 17
- 3.2 Ring-oscillator based impulse generator . . . 18
- 3.3 Parallel LC resonator based impulse generator . . . 18
- 3.4 Triangular impulse generator . . . 19
- 3.5 Negative g_m impulse generator . . . 20
- 3.6 True-differential ring-oscillator impulse generator . . . 21
- 3.7 Two-quadrant voltage square impulse generator . . . 23
- 3.8 Comparison . . . 24

4 Proposed architecture 27
- 4.1 System-level overview . . . 27
- 4.2 Building-blocks . . . 28
  - 4.2.1 Adjustable glitch generator . . . 28
  - 4.2.2 High-frequency differential ring-oscillator . . . 29
  - 4.2.3 Output amplifier and pulse-shaping filter . . . 32
- 4.3 Physical implementation . . . 36

4.4 Results 37
4.4.1 Process corners analysis 40

5 Conclusion and future work **45**
5.1 Achievements 45
5.2 Future work 46

A Circuit Schematics **47**

B Circuit physical implementation **57**

References **63**

List of Figures

1.1 U.S. total expenditure on health. . . . 2
1.2 Accent RF Pacemaker. . . . 3
1.3 Integrate-and-fire signals 4

2.1 Direct I/Q conversion. . . . 8
2.2 Modulation loop using divider control. . . . 8
2.3 Narrow band OOK transmitter. . . . 9
2.4 FCC approved UWB spectrum. . . . 10
2.5 PSD of the higher-order derivatives of the Gaussian impulse. . . . 11
2.6 PSD of the fifth order derivative of the Gaussian impulse for UWB. . . . 11
2.7 Fifth derivative of the Gaussian impulse shape. . . . 12
2.8 A typical ultra-wideband DSSS system. . . . 12
2.9 The multi-band OFDM frequency plan. . . . 13
2.10 Types of IR-UWB modulation. . . . 14

3.1 Delay based impulse generator. . . . 17
3.2 Ring-oscillator based impulse generator. . . . 18
3.3 Parallel LC resonator based impulse generator. . . . 19
3.4 Triangular impulse generator. . . . 20
3.5 Negative gm impulse generator. . . . 21
3.6 True-differential ring-oscillator based impulse generator block diagram. . . . 22
3.7 True-differential ring-oscillator 22
3.8 Two-quadrant voltage square impulse generator. . . . 23
3.9 Narrow band versus IR-UWB transmitters. . . . 25

4.1 System-level schematic. . . . 27
4.2 Adjustable glitch generator schematic. . . . 28
4.3 Glitch length as a function of A and V_{tun} 29
4.4 Glitch generator consumed energy per pulse as a function of A and V_{tun}. . . . 29
4.5 Glitch output waveform. . . . 30
4.6 High-frequency differential inverters tested. . . . 31
4.7 Differential inverter and ring oscillator testbench. . . . 31
4.8 Oscillator output frequency as a function of V_{osc}. . . . 32
4.9 High-frequency differential oscillator schematic. . . . 32
4.10 Output amplifier. . . . 33
4.11 Output filter. . . . 33
4.12 Output filter transfer function response. . . . 35
4.13 Output waveform and its PSD as function of A_{ctrl}. . . . 35
4.14 Triple-well structure. . . . 36

4.15 Physical implementation. 37
4.16 Schematic versus post-layout results. 38
4.17 Final comparison. 39
4.18 Energy consumption distribution percentage per block. 39
4.19 CMOS Corners. 40
4.20 Post-layout SS corner results. 41
4.21 Post-layout FF corner results. 41
4.22 Post-layout FS corner results. 41
4.23 Post-layout SF corner results. 42

A.1 UWB transmitter top level. 48
A.2 Adjustable glitch generator complete schematic. 49
A.3 Differential inverter complete schematic. 50
A.4 Differential inverter reset complete schematic. 51
A.5 Output amplifier complete schematic complete schematic. 52
A.6 Differential pulse-shaping filter complete schematic. 53
A.7 Pulse-shaping filter single cell complete schematic. 54
A.8 And gate complete schematic. 55
A.9 Inverter gate complete schematic. 56

B.1 UWB transmitter physical implementation 57

List of Tables

2.1 CMOS narrow-band transmitters comparison. 9
2.2 Comparison of narrowband and UWB transceiver design. 15

3.1 CMOS ultra-wide band transmitters comparison. 24

4.1 Ring oscillator architectures comparison. 30
4.2 Schematic versus post-layout results comparison. 38
4.3 Post-layout corner simulations results. 43

Abbreviations

A/D	Analog-to-digital converter
AWGN	Additive white Gaussian noise
BPSK	Binary phase shift keying
CMOS	Complementary metal–oxide–semiconductor
DRC	Design rule check
DSO	Digital sampling oscilloscope
DSSS	Direct-sequence spread spectrum
EIRP	Equivalent isotropically radiated power
FCC	Federal Communications Commission
FF	Fast NMOS and fast PMOS
FS	Fast NMOS and slow PMOS
FSK	Frequency-shift keying
GPS	Global positioning system
IFN	Integrate-and-fire neuron
IR-UWB	Impulse-radio ultra-wideband
LNA	Low-noise amplifier
LTCC	Low-temperature co-fired ceramic
LVS	Layout-versus-schematic
MB-OFDM	Multi band orthogonal frequency-division multiplexing
MB-UWB	Multi-band ultra-wideband
MOSFET	Metal–oxide–semiconductor field-effect transistor
MSK	Minimum-shift keying
NMOS	N-channel metal–oxide–semiconductor transistor
OFDM	Orthogonal frequency-division multiplexing
OOK	On-off keying
PA	Power amplifier
PAE	Power added efficiency
PAM	Pulse amplitude modulation
PEX	Parasitic extraction

PHY	Physical layer
PMOS	P-channel metal–oxide–semiconductor transistor
PN	Pseudo noise
PPM	Pulse position modulation
PRF	Pulse repetition frequency
PSD	Power spectral density
RF	Radio-frequency
SF	Slow NMOS and fast PMOS
SNR	Signal-to-noise ratio
SS	Slow NMOS and slow NMOS
TSMC	Taiwan Semiconductor Manufacturing Company
TT	Typical NMOS and typical PMOS
UMC	United Microelectronics Corporation
UWB	Ultra-wideband
VCO	Voltage controlled oscillator

Chapter 1

Introduction

1.1 Motivation

Previous to 1800, the knowledge of electricity was very limited. However, Egyptians and Greeks knew already that certain type of fishes could deliver electrical shocks to an organism in their aqueous environments [1].

In 1758, Benjamin Franklin made the first experiments with electrical stimulation of paralyzed limbs. In a letter to a scottish physician called Sir John Pringle, he reported that after applying strong sparks to affected limbs, "*they were found more capable of voluntary motion, and seemed to receive strength*" [2]. However, after a few days, apparent changes disappeared and the patients went away, tired of receiving severe shocks. Despite his failure, these experiments mark the beginning of the usage of electricity in biomedical engineering.

Biomedical engineering has undergone substantial development since the late 19^{th} century until nowadays. Some important milestones during this period were:

- **1895**: Wilhelm Röntgen discovered the X-ray while investigating the external effects from the various types of vacuum tube equipment [3]. He received the first nobel prize in physics for this discovery.
- **1903**: Willem Einthoven invented the first electrocardiograph, based on a string galvanometer [4].
- **1928**: Alexander Fleming discovered Penicillin. When he came back from a long weekend, he discovered that on an old plate of bacteria, some growing mold was killing the bacteria [5]. Penicillin and sulfanilamide reduced the main danger of hospitalization: cross infection among patients [1].
- **1929**: Hans Berger recorded the first electroencephalograms from human subjects and discovered the rhythmic Alpha brain waves [6].

- **1930**: Refrigeration permitted blood banks. Until that time, the blood was transfused while it was still warm [1].
- **1970's**: Ultrasound, computed tomography, magnetic resonance imaging systems influence different medical fields: ophthalmology, bones and joints problems detection, cancer detection and treatment.

Today, among many other achievements, it is possible to locate the focal origin of epilepsy with millimetric precision [7] and control prosthetic devices with thought [8].

The improvements made in the last century on hygiene, medicine and nutrition led to an increase of life span but also to a dramatic increase of health costs, in a great part due to efforts to deal with chronic diseases [9]. As a representative example, the United States of America have increased the total expenditure on health from 7.1% to 15.8% of the gross domestic product between 1970 and 2006 as illustrated in figure 1.1. This represents a total investment of more than $2,150 billion dollars on 2006 [10, 11].

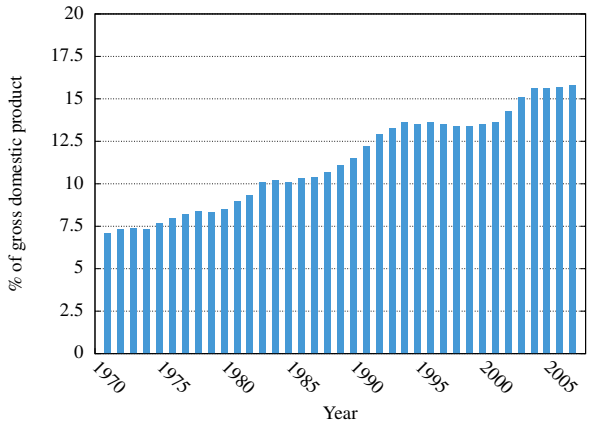

Figure 1.1: U.S. total expenditure on health [10].

New technologies may help to reduce this invoice. As an example, the company St. Jude Medical Inc. has commercialized a wireless pacemaker, illustrated in the figure 1.2. It allows daily remote monitoring and follow-up of patient via Internet, performs real-time electrogram (EGM) and records up to 14 minutes of EGM when encountering one or more programmed conditions [12].

This was the first wireless pacemaker implanted on a U.S. citizen [13]. This technology further improves the patient life quality at the same time that can help reducing treatment costs. In the future these pacemakers may be placed not just on people with slow heartbeat but also on monitoring high blood pressure, glucose monitoring or heart failure.

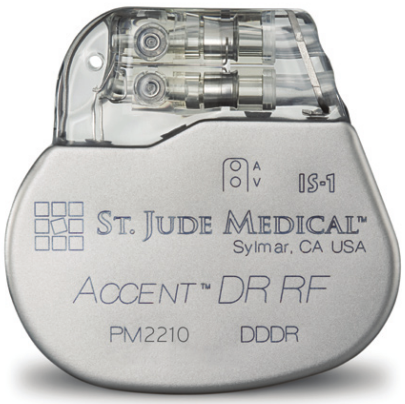

Figure 1.2: Accent RF Pacemaker (Courtesy of St. Jude Medical Inc.).

Another example of state-of-the-art devices already available on the market is the gastrointestinal cameras. A company named Given Imaging Ltd. has commercialized one of these devices called PillCam™. This mechanism is in a form of a capsule that the patient can swallow and while the capsule travels along the digestive tube it takes two pictures each second. The pictures are then transmitted to a vest that the patient wears. This new endoscopy method reduces dramatically the patient discomfort when compared with the traditional endoscopy and it is already available in more than 90 hospitals in the United Kingdom.

Despite distinct functionalities, the designers of these two devices had to overcome a common problem: ultra-low power requirements. In the former case, the pacemaker must work for several years without battery replacement to avoid frequent expensive surgeries. In the second case, although the operating time is just a few hours, the low footprint of the capsule limits the battery capacity and moreover, the image sensors require large quantity of energy to work at a rate of two images per second.

As an example where transmitters can be applied for subcutaneous implants, it is then presented, in the next sub-section, a target application that can take full advantage of the solution proposed solution in this thesis.

1.1.1 Integrate-and-fire system

A major goal of neuroscientists is to better understand the brain processing mechanisms and its complex distributed representations. By tracking several neuronal signals in particular regions of the brain responsible for motor planning or control, it is possible to gather enough information to predict hand trajectories in real time during reaching tasks in awake behaving primates [14, 15]. Authors in [16] propose a 100-electrode neural recording system using a frequency shift keying (FSK) narrowband transmitter. The transmitter is responsible for about 50% of the overall

power consumption of 13.5mW with conventional analog-to-digital converters. The relatively large among of power required prevents the offline utilization of the implant since it needs to be powered from an external inductive link. A different approach is presented in [17] with the inclusion of a rechargeable battery, which can enable the offline utilization of the biomedical implant. In this case, the voltage measured from neurons activity is converted into current and then integrated. The amplitude information is then encoded into an asynchronous digital pulse train as illustrated in figure 1.3.

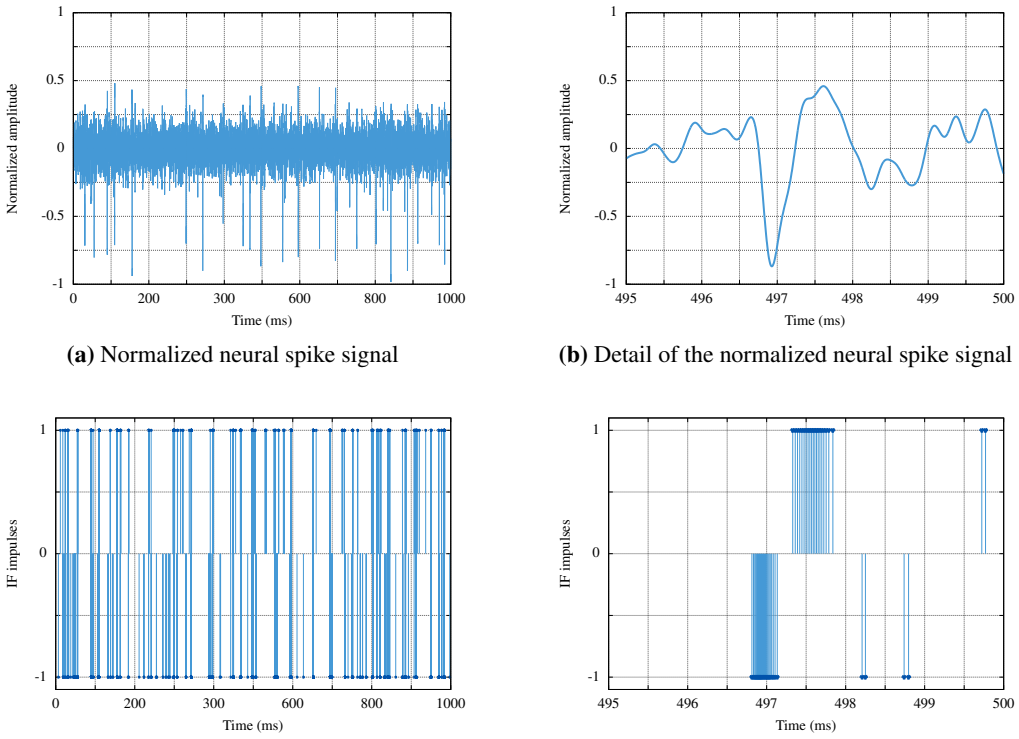

(a) Normalized neural spike signal

(b) Detail of the normalized neural spike signal

(c) Integrate-and-fire system output

(d) Detail of the integrate-and-fire system output

Figure 1.3: Integrate-and-fire signals (Courtesy of Computational NeuroEngineering Laboratory, UFL).

This technique is called Integrate-and-Fire Neuron (IFN). Impulse-radio ultra wideband (IR-UWB) can be applied directly to the IFN system, resulting in a large reduction of the power dissipation since the transmitter can be disabled between neuron spikes. One of the main features of the IFN is that it relies on a conversion from non-constant envelope signals into binary-phase-shifted pulses. These can actually drive an IR-UWB transmitter in a straightforward fashion without any additional circuitry, thus optimizing energy efficiency, which is the main purpose of the hardware in any subcutaneous implant.

1.2 Objectives and proposed solution

Biomedical telemetry provides wireless communication from inside body to outside world and vice versa. Current systems have been designed to communicate with implantable medical devices

such as cardiac pacemakers, neural recording and stimulation, cochlear and retinal implants, etc. To reduce the need of battery exchange and patient discomfort the implants need to operate with very low power consumption.

The main goal of this work is to design a novel ultra-wideband transmitter for subcutaneous biomedical sensing systems. The circuit is proposed to be designed in a CMOS technology, have low power consumption, small footprint and the maximum bit-rate as possible.

The proposed solution consists on a system composed by a ring-oscillator and an output amplifier, both activated by a glitch generator. A band-pass filter is also used for pulse-shaping and frequency spectrum compatibility with wireless regulations. The glitch generator allows for the adjustment of the pulse length and consequently of the output spectrum bandwidth. The ring-oscillator permits the adjustment of the center frequency of the output pulse and the output amplifier is able to adjust the pulses amplitude.

The circuit was implemented in a 90-nm CMOS process with a total area of 675x675μm^2. Corner simulations were also conducted to ensure post fabrication functionality.

1.3 Document organization

In the following chapter some background concepts are presented. Section 2.1 shows some spectrum regulation standards for medical use. Section 2.2 introduces some narrowband transmitter architectures normally used in biomedical implants. Then, in section 2.3 the concept of ultra-wideband is finally presented. A comparison between ultra-wideband and narrowband transmitters in section 2.4 closes this chapter.

The state-of-the-art is presented in chapter 3. Several existing implementation are analyzed from section 3.1 to 3.7 and a comparison between them is shown then in section 3.8.

Chapter 4 presents the proposed architecture in greater detail, beginning with the system-level overview (section 4.1) and the building blocks on section 4.2. The physical implementation is described in section 4.3 and the obtained results in section 4.4.

The conclusions about the developed work and the obtained results are discussed in chapter 5. Section 5.1 enumerates the achievements accomplished and section 5.2 has some suggestions for future improvements and the future work.

To finish this document, the circuit schematics are illustrated in appendix A with all the components dimensions and parameters included. A high-resolution image of the physical implementation is shown in appendix B.

Chapter 2

Background

2.1 Spectrum Regulations for Medical Use

There are two main standards for medical usage: the first is called medical implant communications service (MICS) and can be used in implanted devices to transmit information to the outside world. In 1999, FCC allocated a frequency band for MICS between 402 and 405-MHz [18]. This frequency band has good transmission characteristics within the human body [19]. It is an unlicensed band, although it can be only operated by a medical professional [9]. Regulation limits the equivalent isotropically radiated power (EIRP) to -16-dBm and the channel bandwidth to 300-kHz.

The second standard is the wireless medical telemetry service (WMTS), which can be used to enable wireless communications between an externally worn medical device and other equipments. For example, a portable device can measure the heart rate of a patient and transmit the data to a nearby base station. FCC established this standard in 2000, which defines three frequency bands for WMTS use: 608-614-MHz, 1395-1400-MHz and 1427-1432-MHz [20]. Similarly to MICS, only medical professionals are allowed to operate with equipments in these frequency bands. Regulation stipulates that the maximum field strength allowed for WMTS in the 608 to 614-MHz band is 200-mV/m, measured at 3-m. For operation in the 1395-1400-MHz and 1427-1432-MHz bands, the maximum field strength is 740-mV/m, measured at 3-m. This translates into +11-dBm and +22-dBm of transmit power, respectively.

2.2 Narrowband transmitters

Many modern devices like mobile phones, global positioning system (GPS) receivers and wireless networks use narrow band transmitters and receivers. This section focuses solely on narrowband transmitters for biomedical applications.

Narrowband standards like 802.11 use digital modulation in order to achieve high-spectral efficiency. For example, a direct conversion I/Q transmitter suitable for 802.11 is presented in

figure 2.1. A linear power amplifier must be used, which often has low-power added efficiency [9]. Due to the intrinsic low efficiency, this type of transmitters are not suitable for biomedical implants.

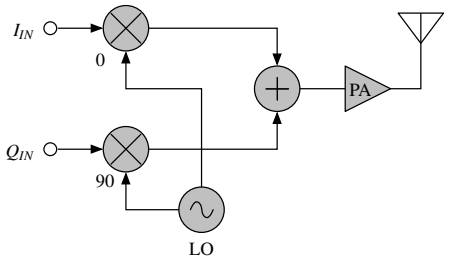

Figure 2.1: Direct I/Q conversion.

Constant envelope modulations like frequency shift keying (FSK) and variants like minimum shift keying (MSK) can drive the power amplifiers close to compression, resulting in higher power added efficiency (PAE) and lower power consumption [9].

With constant envelope phase modulation, one technique to implement the transmitter is to embed the modulation control within a phase locked loop (PLL). A one-point modulation TX loop is shown below in figure 2.2. This scheme removes the two up-converters in figure 2.1. The PLL provides inherent filtering for the modulated signal [9].

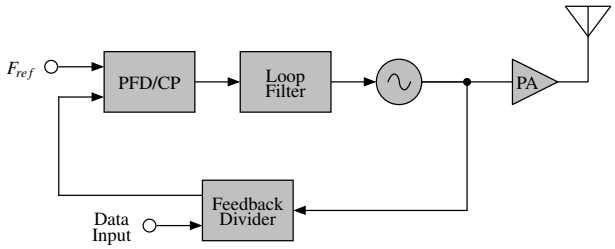

Figure 2.2: Modulation loop using divider control [9].

For the architecture shown in figure 2.2, since the transfer function from the divider to the PLL output is low-pass, the modulation bandwidth is essentially the same as the loop bandwidth. If the channel bandwidth requirement is greater than the loop bandwidth, then the designer must either increase the latter, or consider the voltage controlled oscillator (VCO) modulation [9].

Another way of realizing a low-power transmitter is to use on-off keying (OOK) modulation [21, 22]. With OOK, the transmitter is turned on only when a logic “1” is sent; otherwise the transmitter is turned off. A CMOS OOK transmitter is shown in figure 2.3.

Table 2.1 presents some narrow band transmitter results. The **bold text** represent transmitters for biomedical implants while normal text represent transmitters for body sensor networks. The

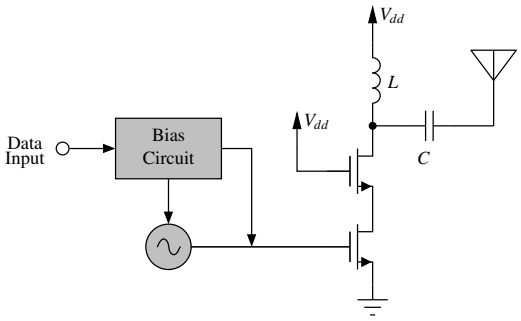

Figure 2.3: Narrow band OOK transmitter [21].

maximum reported bit rate is 17.5-Mbps [23] but except [22] and [24] all the other transmitters have bit rates of tens or hundreds of kbps. Most circuits spend several nJ per transmitted bit.

	Year	Process	Modulation	Transmitter Power (mW)	Maximum Bit-rate (kbps)	Energy per Bit (nJ)
[23]	**2009**	**0.18-μm**	**O-QPSK 400-MHz**	**3.48**	**17500**	**0.2**
[22]	**2009**	**0.5-μm**	**OOK 70-200-MHz**	**-**	**2000**	**-**
[25]	**2009**	**90-nm**	**MSK 391-415-MHz**	**0.35**	**120**	**2.9**
[26]	2008	0.13-μm	FSK 868-915-MHz	2.4	50	48
[24]	2008	0.18-μm	OOK/BFSK 900-MHz	1.91	1000	1.91
[16]	**2007**	**0.5-μm**	**FSK 433-MHz**	**1.65**	**330**	**5**
[27]	2006	0.13-μm	OOK 1.9-GHz	1.35	330	4
[28]	2006	0.13-μm	FSK 2.45-GHz	1.12	500	2.24
[29]	2004	0.25-μm	FSK 820-970-MHz	1.3	20	65

Table 2.1: CMOS narrow-band transmitters comparison.

2.3 Ultra-wideband transmitters

In 2002 the FCC approved the usage of the frequency band between 3.1 and 10.6-GHz for indoor UWB wireless communications systems [30], as illustrated in the figure 2.4.

To ensure compatibility with existing wireless systems, the maximum radiated power is limited to -41-dBm/MHz between 0 - 960-MHz and 3.1 - 10.6-GHz. UWB allows for a low-complexity implementation because the FCC does not restrict the time-domain shape of the transmitted signal. FCC defined UWB as any wireless scheme that occupies a fractional bandwidth W/f_c of at least 20%, where W is the transmission bandwidth and f_c is the band center, or more than 500-MHz of absolute bandwidth [30, 31, 32].

There are two main variants of UWB: multi-band based (MB-UWB) and impulse based. The maximum reported data-rate of MB-UWB is 1-Gbps [33], however this very high bit rate requires

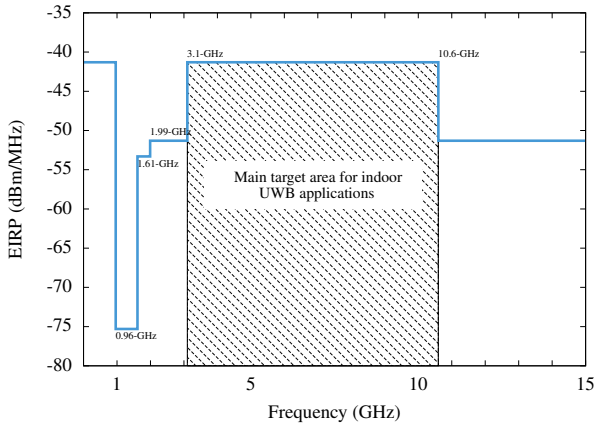

Figure 2.4: FCC approved UWB spectrum [30].

complex hardware, which is not suitable for biomedical implants. For this reason we will focus on IR-UWB in the following sub-sections.

2.3.1 The Gaussian monocycle impulse

As seen in section 2.1, the UWB signal must have at least 500-MHz of bandwidth between 0 and 960-MHz or 3.1 and 10.6-GHz. The most commonly UWB impulse model used in literature is the Gaussian monocycle [34, 35, 36]. There are, however, other methods like modified Hermite polynomials [37].

The Gaussian impulse is defined in equation 2.1 . The constant A is an amplitude normalization constant and σ is related to the width of the impulse.

$$x(t) = \frac{A}{\sqrt{2\pi}\sigma} e^{-\frac{t^2}{2\sigma^2}} \tag{2.1}$$

As demonstrated in [38], the first order Gaussian impulse does not meet the FCC mask. However, the power spectral density (PSD) for the nth order derivative can be determined by equation 2.2.

$$|P_n(f)| = \frac{(2\pi f\sigma)^{2n} e^{-(2\pi f\sigma)^2}}{n^n e^{-n}} \tag{2.2}$$

Figure 2.5 shows the PSD of some derivatives of the Gaussian impulse. It is easy to conclude that at least the fifth derivative has to be taken to meet the FCC mask when the peak coincides with the peak PSD regulated by the FCC.

According to [38], for the fifth derivative, the impulse width is given by equation 2.3.

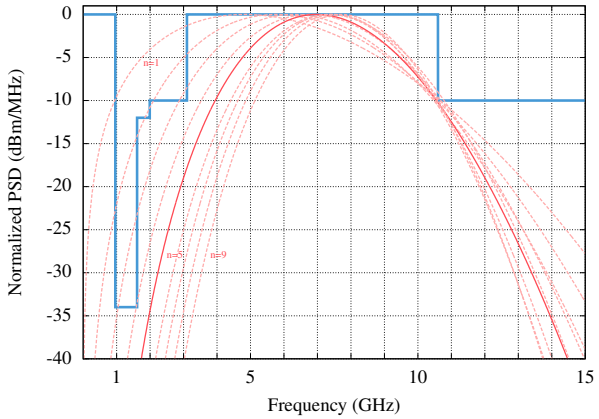

Figure 2.5: PSD of the higher-order derivatives of the Gaussian impulse.

$$T_p \approx 8.5\sigma \tag{2.3}$$

Substituting equation 2.3 in equation 2.2 for n=5 we find the best impulse width that meets the FCC mask. Figure 2.6 shows the normalized PSD for the fifth Gaussian impulse derivative with different impulse widths. As expected, the greater the impulse width, the smaller is its bandwidth.

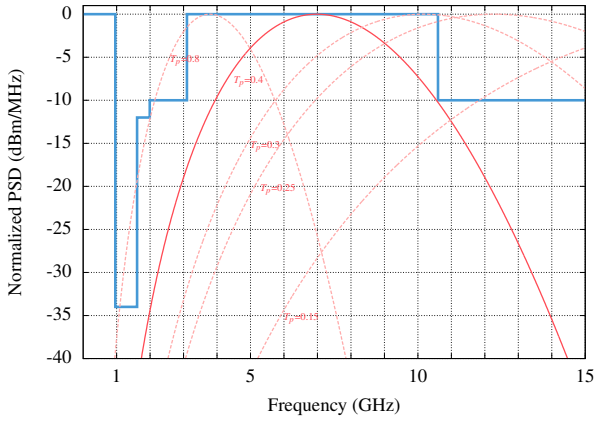

Figure 2.6: PSD of the fifth order derivative of the Gaussian impulse for UWB.

It is possible to observe in figure 2.6 that the ideal impulse width is approximately 400-pS. The time domain representation of the fifth order Gaussian impulse is given by equation 2.4 and it is represented in figure 2.7. The constant A is used to normalize the impulse shape.

$$y(t) = A\left(-\frac{t^5}{\sqrt{2\pi}\sigma^{11}} + \frac{10t^3}{\sqrt{2\pi}\sigma^9} - \frac{15t}{\sqrt{2\pi}\sigma^7}\right) e^{-\frac{t^2}{2\sigma^2}} \tag{2.4}$$

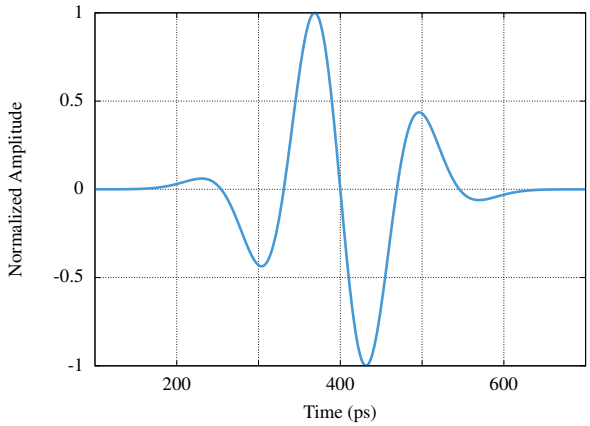

Figure 2.7: Fifth derivative of the Gaussian impulse shape.

Nevertheless, the authors in [39] concluded that if the antenna pulse-shaping effects are taken into account, the FCC rules can be met with only the third derivative.

2.3.2 Direct sequence spread spectrum

Direct sequence spread spectrum (DSSS) is a channel coding technique where low speed information bit stream is mixed with a high-rate continuous string of pseudo-noise (PN) code. The resulting signal at the output of the modulator has a much higher spectral footprint than the original information. A typical DSSS system is shown in figure 2.8.

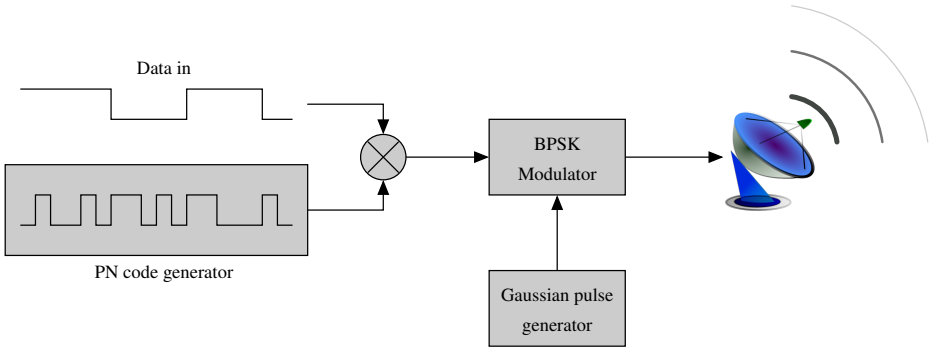

Figure 2.8: A typical ultra-wideband DSSS system.

If more than one PN code sequence is used, it is possible to have different channels for multiuser access. Both single and multiuser architectures are discussed in [40].

The main difference between a narrowband and a ultra-wideband DSSS system is that in the first case, the signal (input data mixed with the PN code) is modulated using a sine wave carrier and in the second using a ultra-wideband signal (i.e. a Gaussian impulse).

In terms of signal-to-noise (SNR) performance, the frequency spreading technique performs no better than a simple BPSK modulated system: the probability of error is only dependent on the

integrated received bit-energy to additive white Gaussian noise (AWGN) spectral density (E_b/N_0) in the transmission band [41]. However, DSSS offers a limited protection against accidental in-band spurious signals, because the de-spreader in the receiver easily removes them. The principles of de-spreading are very simple: mixing the spread sequence a second time with a replica of the spreading code will yield the original information stream. The effect of the de-spreader on a narrowband interferer is exactly the opposite: its energy is spread out over a large bandwidth and can be removed by a simple low-pass filter at the output of the de-spreader. In practice, things get a little bit more complicated: the offset of the spreading sequence generated locally in the receiver must be aligned properly to the spreading sequence in the encoded data stream. Failing to do so will result in a high-frequency noise signal, without a single trace of the original information. Interestingly enough, this property is at the same time the biggest disadvantage but also the biggest strength of DSSS-based systems.

2.3.3 Multi-band orthogonal frequency division multiplexing

Multi-band orthogonal frequency division multiplexing (MB-OFDM) distributes the data over a large number of carriers that are spaced apart at precise frequencies. This spacing provides the orthogonality in this technique, which prevents the demodulators from seeing frequencies other than their own. The benefits of OFDM are high-spectral efficiency, resiliency to RF interference, and lower multi-path distortion.

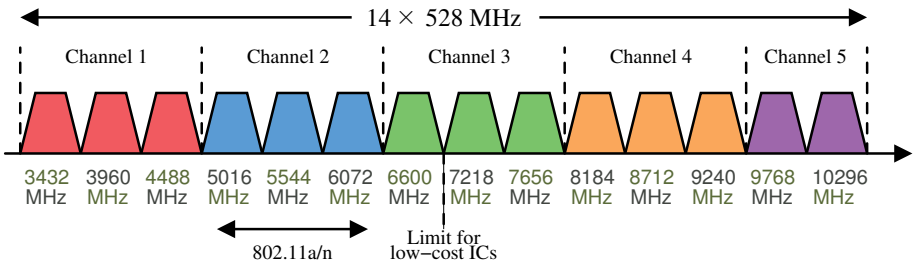

Figure 2.9: The multi-band OFDM frequency plan.

As shown in figure 2.9 there are 14 bands of 528-MHz wide. These bands are distributed for 5 different channels. Authors in [42] concluded that coexistence of 802.11n wireless systems - that operates between 5.15 and 5.7-GHz - causes a severe degradation in the detection performance. In fact, most of the works in OFDM UWB only use the first channel to avoid interferences with 802.11a/n systems and because low-cost integrated circuits can hardly reach frequencies above 6.5-GHz [43].

A representative implementation can be found in [44]. In this article, the authors present an integrated RF transceiver and digital physical layer (PHY) on a single CMOS chip that includes all the active circuitry required for operation in channel #1 (3.1 to 4.8-GHz), and supports both fixed-frequency and frequency-hopping modes in 528-MHz bands.

2.3.4 Impulse-radio

Impulse-radio ultra-wideband (IR-UWB) is based on the transmission of narrow impulses (typically of hundreds of pico-seconds), thereby spreading the energy of the radio signal by the maximum bandwidth as possible between FCC mask limits. Due to its significant bandwidth, an impulse radio based system may accommodate many users, even in multi-path environments [45].

The most commonly used modulations in IR-UWB are:

- **Pulse position modulation (PPM)**: For a single-user system with PPM signaling, bit "1'" is represented by a impulse without any delay and bit "0" is represented by a impulse with a delay τ relative to the time reference.
- **Pulse amplitude modulation (PAM)**: In PAM, the input signal modulates de output impulse amplitude.
- **Binary phase shift keying (BPSK)**: In BPSK modulation, the phase of the UWB impulse is shifted 180 degrees in accordance with a digital bit stream.
- **On-off keying (OOK)**: for OOK signaling, information bit "1" is represented by the presence of a impulse and no impulse is sent for bit "0".

The four types of modulations described above are illustrated in the figure 2.10.

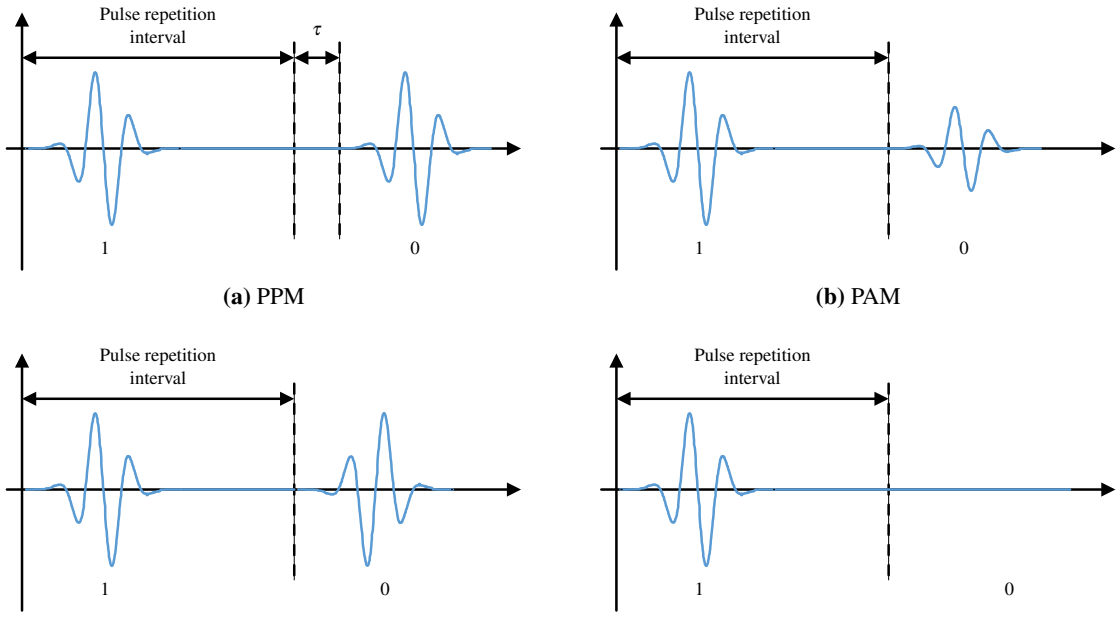

(a) PPM **(b)** PAM **(c)** BPSK **(d)** OOK

Figure 2.10: Types of IR-UWB modulation [31].

2.4 Ultra-wideband versus narrowband transmitters

As demonstrated by Ramirez-Mireles in [46] and [47], the major narrowband inconvenience of fading is no longer important for UWB: it is only 3 - 4-dB for UWB in contrast to 30 - 60-dB for narrowband. Another conceptual difference is the necessity to consider the per-path impulse distortion that is neglected in Turin's multi-path channel model. Each path will have its own impulse response (IR) of frequency transfer characteristics that is frequency dependent [48].

On the other hand, the main disadvantage of UWB comparing with narrowband systems, is the fact that antennas can be modeled as the front-end pulse-shaping filter. In UWB systems, impulse-waveform if often present [49]. Table 2.2 presents a short comparison between ultra-wideband and narrowband transceivers.

	Ultra-wideband	**Narrowband**
Antennas	Small antenna design with gain and wide bandwidth. Low-impedance antenna and good wideband matching with few components is difficult. Antenna and front-end co-design is necessary.	Small antenna with high Q and good gain is easily achievable; 50Ω impedance easy to match; Antenna and front-end can be designed independently.
RF front-end	Wideband LNA are power consuming and hard to match, the AGC is part of the front-end; Relaxed requirement on linearity; Partial filtering is achieved by the antenna.	Narrowband LNA are easy to match; Non constant envelope modulation (e.g. OFDM) need very high linearity; Filtering is needed to satisfy out-of-band emissions.
Intermediate frequency	No need.	AGC, Mixers, RF oscillators, PLL.
Analog baseband	Very high bandwidth A/D converters; Extended-time sampling techniques; Digital sampling oscilloscope techniques (DSO).	Small bandwidth A/D converter.
Digital baseband	Coherent detection with fine time resolution; Precise time references.	Non-coherent detection.
Other aspects	External CW jammer; Complex channel models.	Load-pull; LO leakage; LO pulling by PA; Narrow channels are well characterized (fading models).

Table 2.2: Comparison of narrowband and UWB transceiver design [50].

It is possible to conclude observing the table 2.2 that ultra-wideband transmitters are much easier to implement than narrowband ones 2.2.

Chapter 3

State of the art

3.1 Delay based impulse generator

Figure 3.1 presents the delay-based impulse generator [36]. The NAND gate is low logic level when both inputs are high, and the NOR is high when both inputs are low. This only happens in the transition of the input inverters due to the propagation time. In the first stage M_1 is activated, then M_2, M_3 and finally M_4. For each positive edge of the strobe signal, only one impulse is generated.

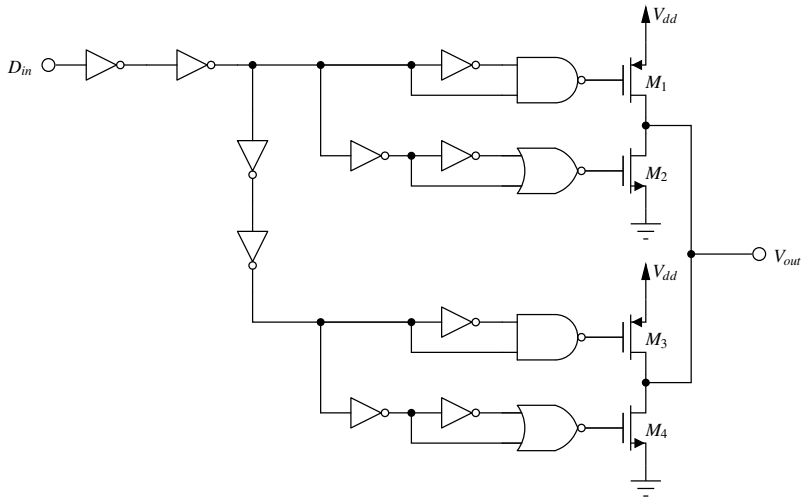

Figure 3.1: Delay based impulse generator [36].

A prototype was fabricated with AMI 0.5-μm CMOS process. The measured impulse has a width of 2.4-nS and the peak-to-peak amplitude of 148-mV, against the 1.6-nS width and 816.5-mV peak-to-peak amplitude obtained in simulation. The average power consumption is 1.16-mW when it is driven by a 20-MHz input signal.

The authors justify the different between the simulated and the measured results with the argument that the parasitic resistance of poly capacitor was not taken in account into simulation.

Beyond the fact that the simulated and measured results do not match, at least reasonably, the proposed solution lacks a calibration mechanism to reduce the fabrication derivations.

The power consumption of 1.16-mW with a bit-rate of 20-Mbps translates into a energy consumption of 58-pJ per impulse.

3.2 Ring-oscillator based impulse generator

Figure 3.2 presents another UWB impulse generator [35]. It is based in a common single-ended ring-oscillator circuit that can be turned on/off by transistor M_4 that is driven by a glitch generator. The ring-oscillator has feedback resistors to increase the resulting frequency. Transistors M_7 and M_8 are responsible for the power amplification and output driving. The circuit also has a high-pass filter, not shown in the figure, to comply with FCC spectral mask.

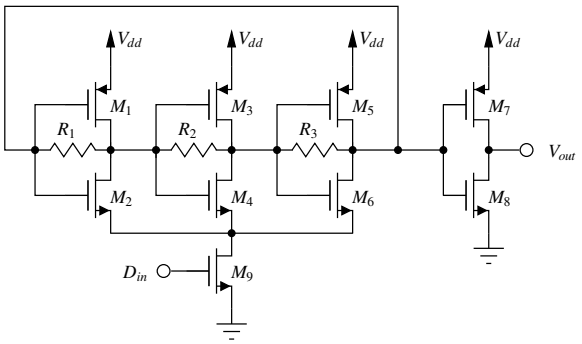

Figure 3.2: Ring-oscillator based impulse generator [35].

The circuit was fabricated using a 0.18-μm CMOS process. The impulse has 500-pS of width and a -10-dB bandwidth of 4.5-GHz from 5.9 to 10.4-GHz. The average power consumption is 1.38-mW for a impulse repetition frequency of 50-MHz and 2.1-V supply voltage. This corresponds to 27.6-pJ of energy consumption per pulse.

The measurement results demonstrated low-power dissipation, high-peak amplitude, and low jitter performance. However it lacks a calibration circuit like the previous one. For example, it could be possible to add varactors in the ring oscillator loop in order to calibrate the central output frequency.

3.3 Parallel LC resonator based impulse generator

In figure 3.3 a parallel LC resonator based impulse generator is presented [51]. When the enable signal is zero, the capacitor C is charged through M_1. When the input signal switches to V_{dd}, the transistor M_2 closes the oscillator circuit composed by inductance L and capacitor C. The circuit will oscillate until its energy is dissipated due to the parasitic resistances in the circuit. The

oscillation frequency is given by the *LC* natural resonant frequency, which can be calculated using equation 3.1.

$$f = \frac{1}{2\pi\sqrt{LC}} \tag{3.1}$$

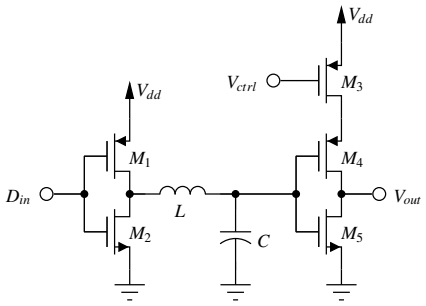

Figure 3.3: Parallel LC resonator based impulse generator [51].

The center frequency was 3.8-GHz and the bandwidth nearly 1.5-GHz. It consumes 7.30-mW with a pulse repetition frequency (PRF) of 200-MHz resulting in a energy consumption per pulse of 36.5-pJ. The major drawback of this solution is the relatively narrow bandwidth and low center frequency, which easily can drift to less of 3.1-GHz due to fabrication deviations. This can lead to FCC mask non-compliance.

3.4 Triangular impulse generator

Another approach is presented in figure 3.4. In this case, the authors developed a triangular impulse generator compatible with BPSK modulation [34]. The impulse generator can be connected directly to an integrated antenna or to a power amplifier when an external antenna is used.

The clock and data signals are given directly to the impulse generator, which generates the biphase modulated pulses of 500-ps duration and 8-GHz center frequency. Four impulse generator cells are concatenated to form a chain. Each impulse generator cell generates a 125-ps monocycle impulse that when combined together form the output pulse.

When the data is “1”, the upper left transistors of the impulse generator cell are turned on at the falling edge of the clock and the output is pulled to V_{dd}. As the clock passes through the first inverter, the diagonally opposite path of the impulse generator cell turns on and at the rising edge of the clock, the output is pulled down to ground. When the clock passes through all four impulse generator cells, a 500-ps pulse is generated. Similarly, a 180 degree phase shifted pulse is generated when the data is “0”, but at the opposite clock transition. Since the “1” and “0” pulses

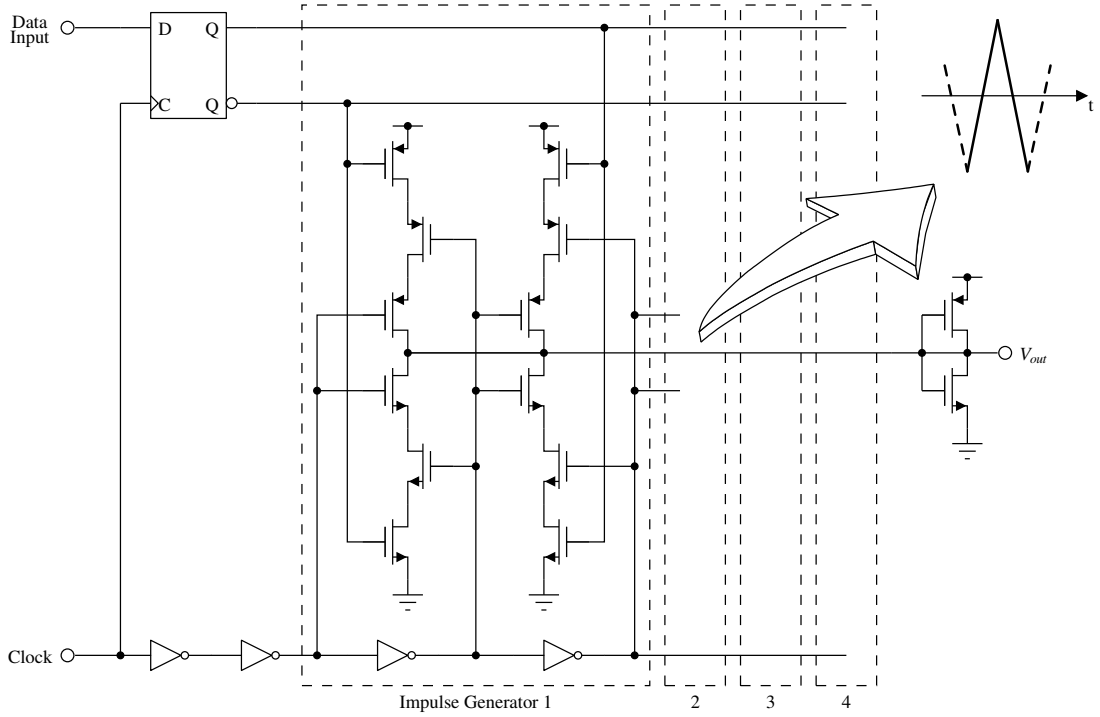

Figure 3.4: Triangular impulse generator [34].

are generated at different clock timings, the clock is inverted at every data transition, keeping the pulse position constant for "1" and "0" pulses. This gives rise to a problem of charge sharing.

The integrated circuit was fabricated in a 0.18-μm CMOS process. Measured results show that the transmitter consumes 12-pJ/b to achieve a maximum pulse repetition rate of 750-Mb/s. This is the fastest transmitter found in the literature.

3.5 Negative g_m impulse generator

The architecture presented in figure 3.5 shows a negative g_m impulse generator [52]. A switched capacitor bank is used for the frequency band selection. Two switches, SW_1 and SW_2, control the tank and VCO current source, respectively. When SW_2 is on and SW_1 is off, pulses are generated at the output. An inverter is used to make square pulse trains at node A and B with 180 degrees of phase difference to drive SW_2 and SW_1, respectively. When one switch is on, the other is off and vice versa. The triangular-enveloped pulse is supposed to provide more than 20-dB of side-lobe rejection, which is important for adjacent channel interference suppression in multi-band systems. The key idea to obtain the triangular-like pulse shape is to turn off the oscillation before its steady-state. The high performance pulse with maximum side-lobe rejection is achieved when the rise time is equal to the fall time.

This IR-UWB transmitter was implemented in 0.18-μm CMOS process. It is able to transmit information using OOK modulation and operates in three different bands of 528-MHz between

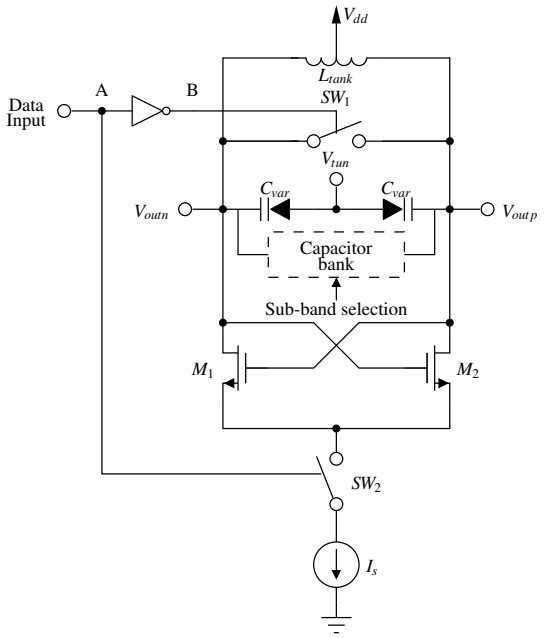

Figure 3.5: Negative gm impulse generator [52].

3 and 5-GHz. Measured pulse PSD fully satisfies FCC mask with more than 20 dB of side-lobe suppression. The total transmitter dissipates only dynamic current in burst mode with 18-pJ of energy consumption per pulse.

This circuit presents a simple architecture. However, the VCO commutation takes much time and thus, this transmitter is not suitable for high bit-rate operation.

3.6 True-differential ring-oscillator impulse generator

Figure 3.6 presents a true-differential ring-oscillator impulse generator diagram block [53]. The triangular impulse generator and the ring oscillator are activated simultaneously. The triangular signal is multiplied with the carrier created by the oscillator, resulting in an up-converted triangular pulse at the output. The triangular waveform has a duration that can be adapted in accordance with the desired bandwidth. A gating circuit activates the ring oscillator when a pulse must be transmitted, avoiding useless power consumption between the pulses. The choice of a ring type oscillator was taken since its startup time is very low, while the high phase-noise problem is obviously not an important issue in the generation of wide-band signals.

The ring-oscillator activation circuit uses the same principle as for the PPM. By making its charging current twice the one required in the triangular pulse generator, the ring-oscillator operates during the whole duration of the pulse. The carrier generator is a three-stage differential ring oscillator, as shown in figure 3.7. Ring oscillators typically have very low startup times due to their low quality factors. Transistors M_6 and M_7 are used to force initial conditions. By forcing

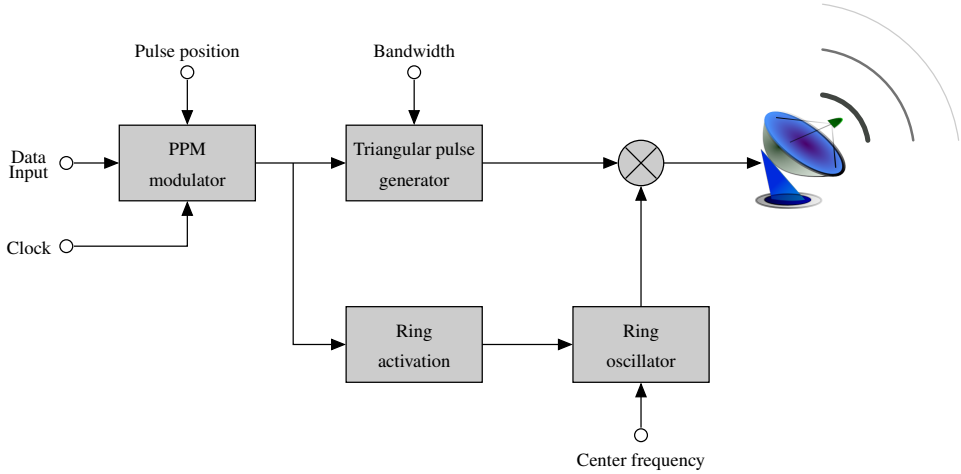

Figure 3.6: True-differential ring-oscillator based impulse generator block diagram [53].

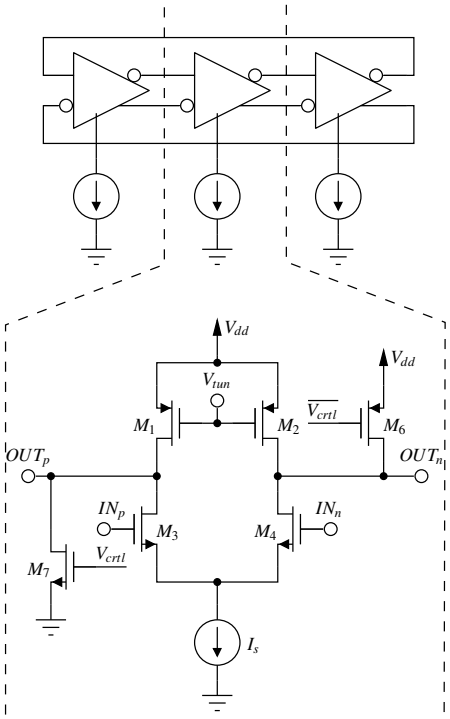

Figure 3.7: True-differential ring-oscillator [53]

initial conditions on each stage of the ring oscillator, the startup time is further decreased. In this way, the oscillator reaches its steady-state in less than two cycles.

This impulse generator has been implemented in a 0.18μm CMOS technology. Most of the transmitter building blocks are switched off between the pulses. The energy consumption is 50-pJ per pulse at 40-MHz pulse repetition frequency.

3.7 Two-quadrant voltage square impulse generator

A two-quadrant voltage square impulse generator is shown in figure 3.8. The square circuit is composed by transistor M_1 and resistor R. When M_1 is biased in the saturation region, the drain voltage of M_1 can be written as

$$V_{sqrt} = V_{in} - R\frac{K}{2}(V_{in} - V_{th}))^2 \tag{3.2}$$

If choosing

$$R = \frac{2}{KV_{th}} \tag{3.3}$$

then 3.2 becomes

$$V_{sqr} = -\frac{1}{V_{th}}\left(V_{in} - \frac{3V_{th}}{2}\right)^2 + \frac{5V_{th}}{4} \tag{3.4}$$

where $V_{th} < V_{in} < 2V_{th}$ should be satisfied to keep M1 in the saturation region. Thus, a two-quadrant voltage square circuit is implemented as indicated by [54].

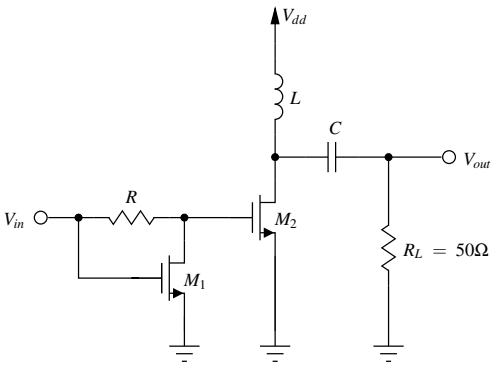

Figure 3.8: Two-quadrant voltage square impulse generator [55].

A prototype of the integrated circuit has been fabricated in a 0.18-μm CMOS process with an low-temperature co-fired ceramic (LTCC) antenna. The measured prototype impulse radio achieved a data rate of 165-Mb/s over an wireless channel with a length of 20-cm and a transmitter power consumption of 21-mW.

3.8 Comparison

Table 3.1 shows the state-of-the-art UWB transmitters specifications. For comparison with the narrowband transmitters, the average consumed power was calculated with a bit rate of 2-Mbps. The figures of merit for UWB transmitters considered herein are the pulse amplitude, the pulse width, the maximum bit rate and of course the energy consumption per bit.

	Year	Process	Pulse Amplitude (mV)	Pulse Width (pS)	Average Power @ 2Mbps (μW)	Maximum Bitrate (Mbps)	Energy per Pulse (pJ)
[35]	2009	0.18-μm	670	500	56	-	28
[51]	2009	65-nm	400	600	73	200	36.5
[34]	2009	0.18-μm	120	500	82	750	41
[52]	2007	0.18-μm	180	3500	36	100	18
[36]	2005	0.5-μm	148	2400	120	200	58
[53]	2005	0.18-μm	200	1100-4500	100	40	50

Table 3.1: CMOS ultra-wide band transmitters comparison.

It is possible to observe that [52] requires less energy per transmitted bit than all the other implementation but at the same time its pulse amplitude is the smallest. Authors in [34] reported the maximum bit rate of 750-Mbps.

Results in tables 2.1 and 3.1 are summarized in figure 3.9. This figure justifies entirely the usage of UWB transmitters for biomedical implants. It is clear that for the same average power consumption, a UWB transmitter is capable of transmitting a much larger amounts of data.

The maximum reported data-rate for IR-UWB is 750-Mbps against the 24-Mbps for Bluetooth 3.0 for example. However, despite the greater data rate capacity, IR-UWB transmitters require less power consumption, are simpler and cheaper than narrow band transmitters. This makes IR-UWB the better choice for biomedical implants transmitters.

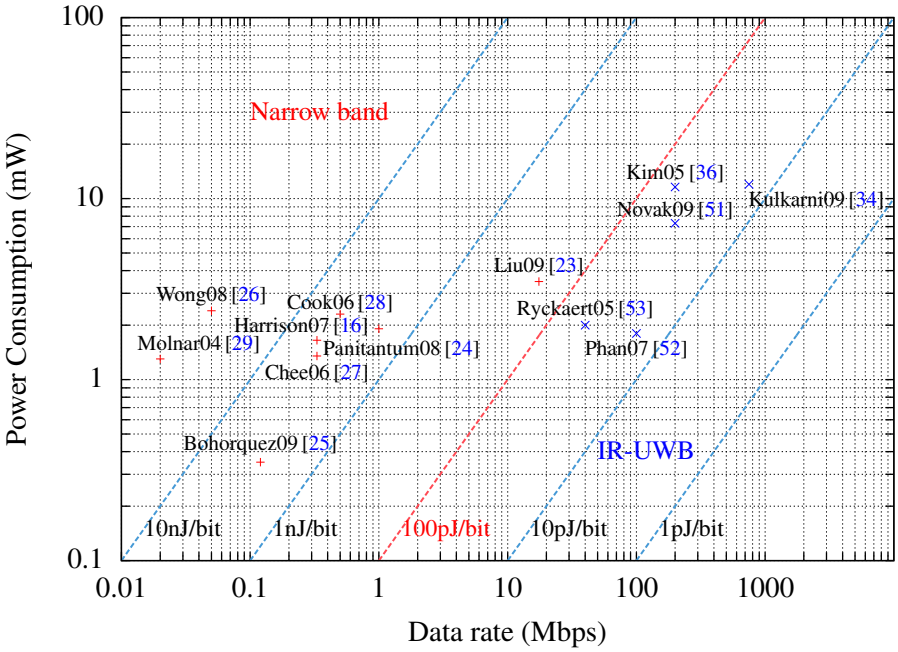

Figure 3.9: Narrow band versus IR-UWB transmitters.

Chapter 4

Proposed architecture

4.1 System-level overview

Figure 4.1 illustrates the proposed architecture. The core of the circuit is the differential ring-oscillator composed by the inverters INV_1 and INV_2. It defines the center frequency of the output signal. Therefore, it is expected to be capable of operating at frequencies of at least 6-GHz, since the objective is to occupy the maximum spectrum as possible, defined between 3.1 and 10.6-GHz. This way the probability of detection is maximized.

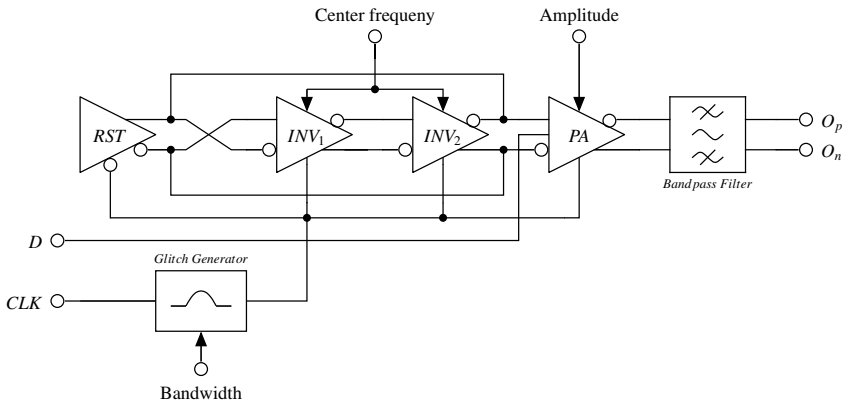

Figure 4.1: System-level schematic.

The output amplifier isolates the ring oscillator from the output load. It is also responsible for the output signal amplitude and respective power, and defines the output signal phase depending on the input data. It is followed by a bandpass filter responsible for shaping the output pulse.

As concluded in sub-section 2.3.1 the pulse length has only some hundreds of pico-seconds. For this reason, both the oscillator and the power amplifier must be activated by a glitch generator. A glitch is a pulse with a very short duration, normally undesired in electronic circuits.

This transmitter was designed for BPSK modulation. However, it is capable of operating with OOK, PPM and even PAM. For the last three modulations, the data input must be fixed in one

logic level. Then, for OOK and PPM the output data is modulated using the clock signal. For PAM, the output data is modulated by changing the gain of the output amplifier and applying a positive clock transition on each bit. This is another advantage of this architecture when compared with ones analyzed in the previous chapter.

The next section describes the above blocks in greater detail.

4.2 Building-blocks

4.2.1 Adjustable glitch generator

The adjustable glitch generator was originally introduced in [56] and improved in [57]. The proposed circuit, presented in figure 4.2, is an adaptation of [57] where it was added a bypass signal *BP*. This signal allows for the external control and calibration of the transmitter.

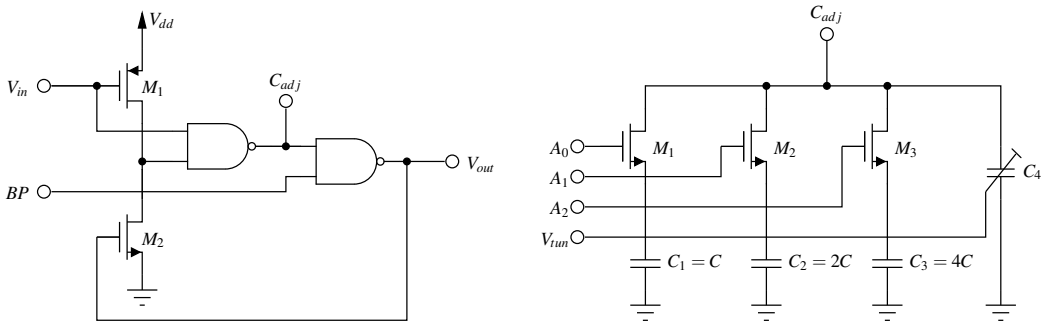

(a) Glitch generator **(b)** Binary weighted capacitance array

Figure 4.2: Adjustable glitch generator schematic.

The resulting pulse width can be approximated by equation 4.1.

$$t_p = \frac{(t_r + t_f)_{NAND_1} + (t_r + t_f)_{NAND_2}}{2} \tag{4.1}$$

The rise and fall times of the second NAND are fixed since the load itself is fixed. However, it is possible to adjust the rise and fall times of the $NAND_1$ with the adjustment of the capacitors C_1 to C_4. C_1 to C_3 together with transistors N_1 to N_3 form a binary weighted capacitance array, which can be digitally controlled by inputs A_0 to A_2. C_4 is a varactor (adjustable capacitance) and it provides a fine tuning for the desired glitch width.

Figure 4.3 illustrates the glitch pulse width as a function of A and V_{tun}. It is possible to achieve any time width between 218 and 394-pS. Note that there is some overlap between two consecutive curves in order to ensure a continuous tune range.

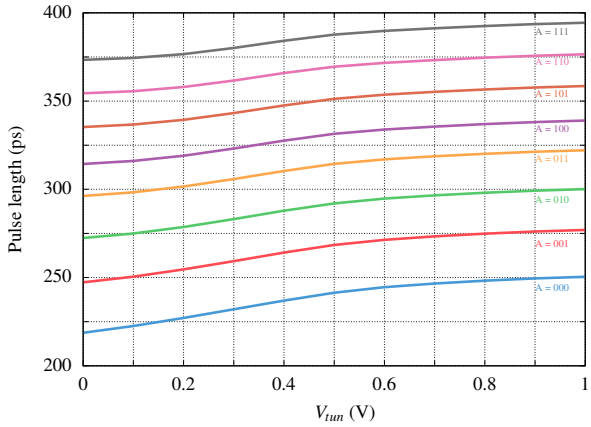

Figure 4.3: Glitch length as a function of A and V_{tun} (C_L = 2-pF).

This block is responsible by the consumption of approximately half of the total energy consumption, since it has to drive all the other blocks. The load capacitance was obtained through measurement and is approximately equal to 2-pF. Figure 4.4 shows the energy consumption per bit. As expected, the longer the pulse width, the higher the energy consumption is.

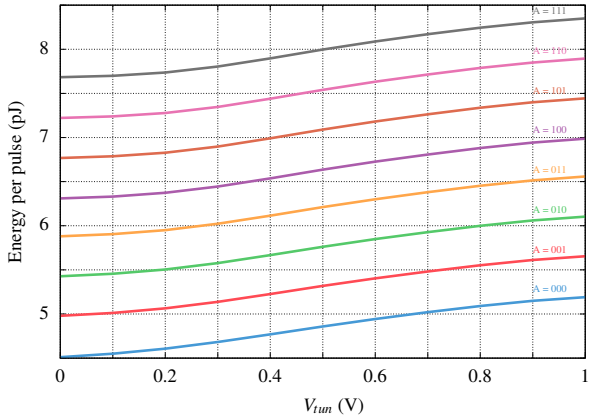

Figure 4.4: Glitch generator consumed energy per pulse as a function of A and V_{tun}(C_L = 2-pF).

Finally, figure 4.5 shows three output glitches with different calibrations. The output pulses are very sharp, the transitions are very fast and the pulse amplitude is almost rail-to-rail.

4.2.2 High-frequency differential ring-oscillator

Table 4.1 presents a small comparison between three different types of architectures of ring oscillators 4.1.

Most of the pulse-based architectures found in literature are single-ended. However, single-ended architectures are most susceptible to amplitude coupling interference from supply/substrate.

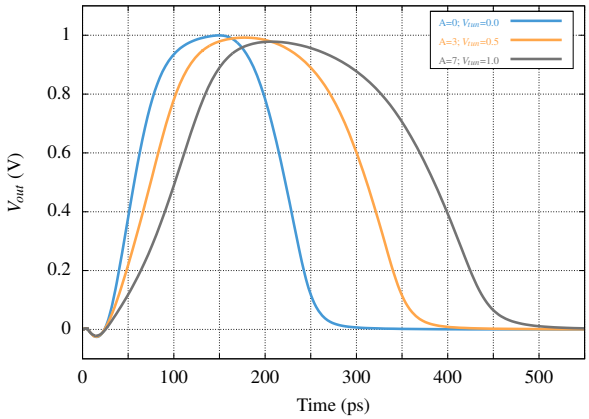

Figure 4.5: Glitch output waveform (C_L = 2-pF).

To avoid this kind of interferences and to reduce the jitter noise, it is proposed a fully-differential configuration from the impulse generation to the antenna.

	Single-ended	**True-differential**	**Pseudo-differential**
Power-consumption	Only draws power in signal transitions. Consume increases with the frequency.	Static and dynamic consumption.	Similar to single-ended.
Signal Amplitude	Rail-to-rail.	Smaller signal swing.	Rail-to-rail.
Interference immunity	Very susceptible. High jitter.	Good immunity. Low jitter.	Some rejection of amplitude coupling interference but limited immunity to delay modulation.
Number of stages	Must be odd. No quadrature outputs.	Even or odd. Quadrature outputs.	Even or odd. Quadrature outputs.

Table 4.1: Ring oscillator architectures comparison [58].

True-differential ring-oscillators are more power demanding than the other architectures but less sensitive to interferences. Figure 4.6 introduces two different approaches of true-differential inverters. Please note that NMOS transistors M_6 have a large W/L ratio and therefore operate as switches. On the other hand, PMOS transistors M_1 work as a current source and they are used to adjust the output frequency of the ring-oscillator.

In figure 4.6a, transistors M_2 and M_3 act as two cross-coupled inverters since when one branch is set to logic level “0”, the other is forced to level “1”. In figure 4.6b two PMOS transistors were added witch increase inverter speed.

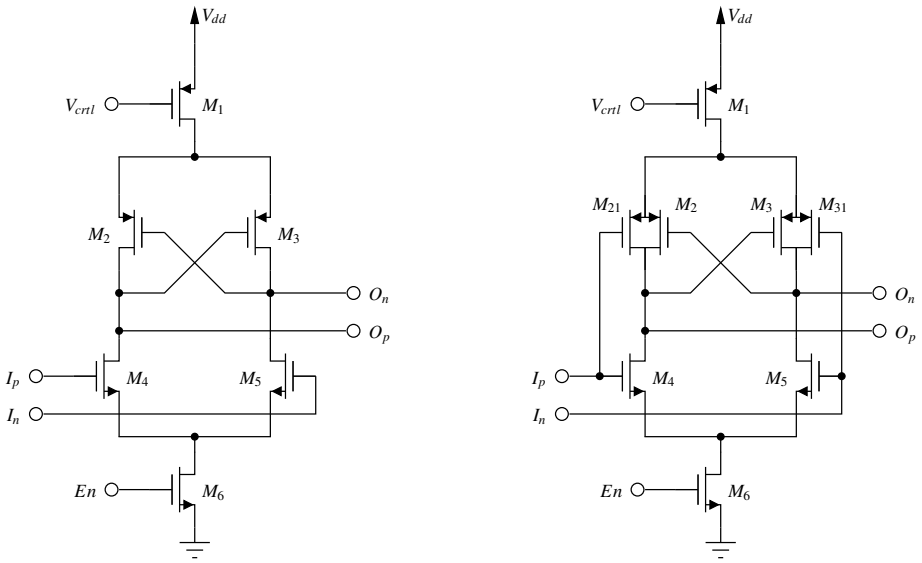

(a) McNeill09 [58] based architecture **(b)** Park01 [59] based architecture

Figure 4.6: High-frequency differential inverters tested.

The inverters of figure 4.6 were tested on a two-stage ring-oscillator testbench as shown in figure 4.7.

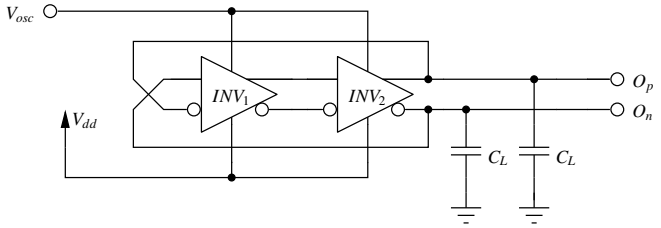

Figure 4.7: Differential inverter and ring oscillator testbench.

As shown in figure 4.8, the McNeill09-based [58] inverter has a lower oscillation frequency but on the other hand allows for a greater adjustment range through V_{osc}. Transistors M_{21} and M_{31} of the Park01-based [59] inverter increase the ring feedback and the frequency. In fact, with larger W/L ratios in this transistors it is possible to obtain more than 13-GHz of oscillation frequency, but the frequency adjustment range decreases dramatically. In figure 4.8b when V_{osc} passes 500-mV, the oscillation stops. In addiction, Park01 ring oscillator consumes more energy than McNeil09.

After the comparison of the advantages and disadvantages of the two architectures, the McNeill09-based was chosen.

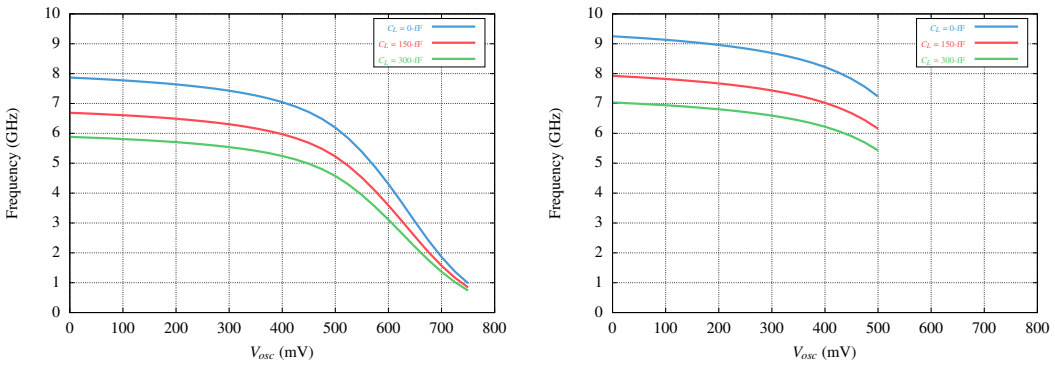

(a) McNeill09 frequency adjustment

(b) Park01 frequency adjustment

Figure 4.8: Oscillator output frequency as a function of V_{osc}.

Figure 4.9 illustrates the complete ring oscillator schematic, including the reset circuit composed by the transistors M_1 and M_{12}. These transistors are responsible for ensuring a know state when the enable signal is not active (i.e. $En = 0$).

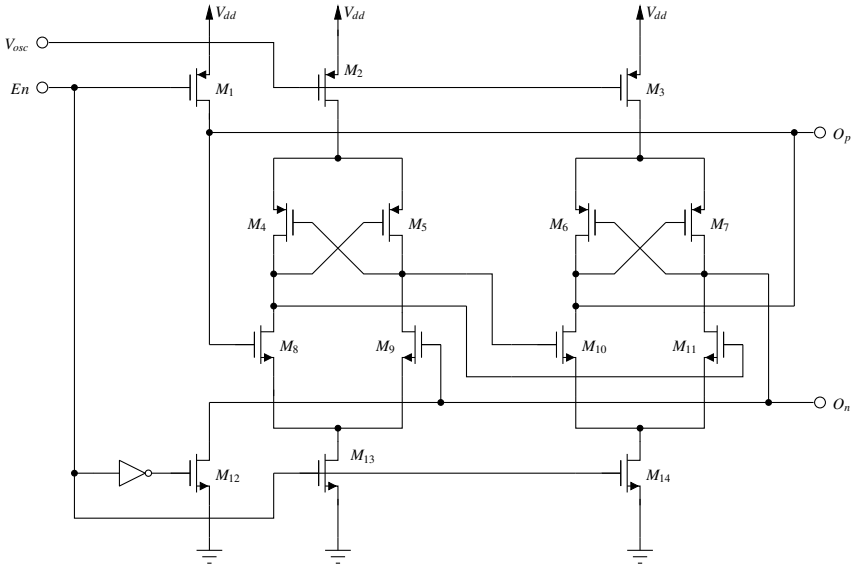

Figure 4.9: High-frequency differential oscillator.

4.2.3 Output amplifier and pulse-shaping filter

The developed output amplifier is presented in figure 4.10. It has two different branches (M_3-M_4 and M_5-M_6) that are activated in accordance with the input data. When the input data is "0" and the enable is "1", the pair M_5-M_6 is activated. Otherwise, when the input data is "1" the pulse is generated by M_3-M_4 with 180 degrees phase difference.

Transistors M_7 and M_8 act as on-off switches controlled by the enable and data inputs. In the first implementation attempt a series of two transistors on each branch were used instead of

M_7 and M_8. One for the data input and the other for the enable signal. However, due to the low performance of this solution for high-frequency signals, the two transistors in series were replaced by the transistors M_7, M_8 and the control logic that activates them.

The two transistors, M_1 and M_2, restrict the maximum current in each branch and consequently the output amplitude.

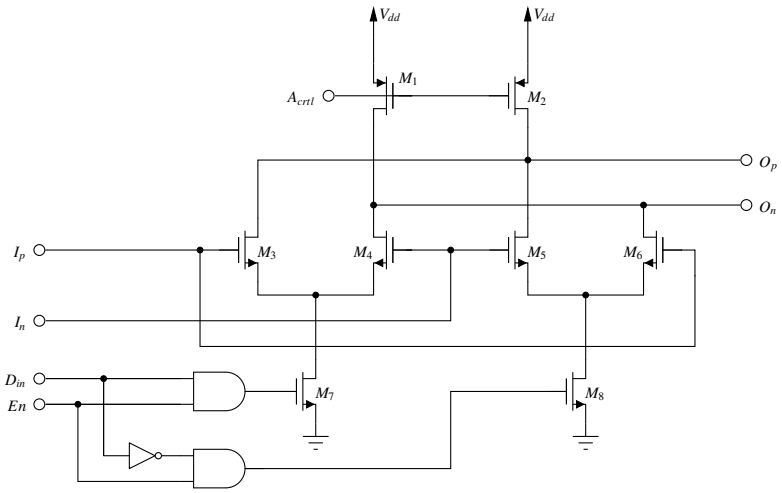

Figure 4.10: Output amplifier.

The output amplifier generates an impulse with a center frequency defined by the ring-oscillator. To ensure that the output impulse meets the FCC mask presented in section 2.3, a filter must be added between the output amplifier and the load/antenna. The antenna itself will act as a pulse-shaping filter. However, this internal filter, ensures that the FCC mask will be respected for different antenna models.

Figure 4.11a shows a conventional T-section filter in which the series impedance Z_1 is a series resonant circuit (L_1 and C_1) while the shunt impedance Z_2 is a parallel tuned circuit (L_2 and C_2). Components L_1, C_1, L_2 and C_2 are so chosen that the series resonance frequency of the series arms equals the parallel resonance frequency of the shunt arm as demonstrated in [60].

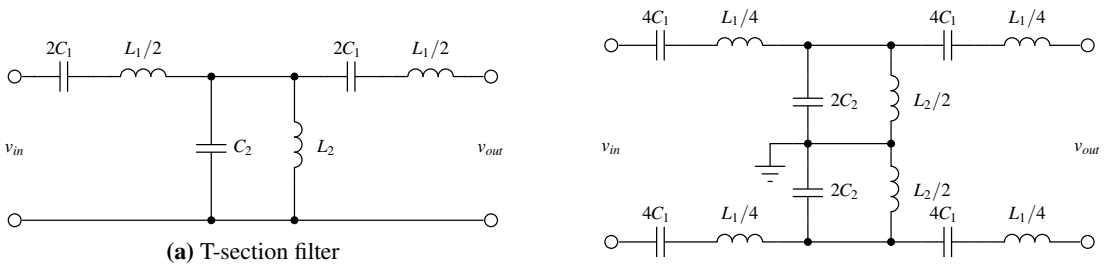

(a) T-section filter

(b) Balanced T-section filter

Figure 4.11: Output filter.

Hence, after some mathematical manipulation, the components values are found to be:

$$L_1 = \frac{Z_0}{\pi(f_2 - f1)} \tag{4.2}$$

$$L_2 = \frac{Z_0(f_2 - f_1)}{4\pi f_1 f_2} \tag{4.3}$$

$$C_1 = \frac{f_2 - f_1}{4\pi f_1 f_2 Z_0} \tag{4.4}$$

$$C_2 = \frac{1}{\pi(f_2 - f1)Z_0} \tag{4.5}$$

The cut-off frequencies (f_1 and f_2) are so chosen to be contained in the FCC mask limit (3.1 to 10.6-MHz) with a safety margin of 500-MHz on each side. Since this is a differential circuit, the output impedance (Z_0) is equal to 100-Ω. Hence, the components are finally dimensioned:

$$L_1 = \frac{100}{\pi(10.1 - 3.6) \times 10^9} = 4.90\text{-}nH \tag{4.6}$$

$$L_2 = \frac{100 \times (10.1 - 3.6) \times 10^9}{4\pi \times 10.1 \times 3.6 \times 10^{18}} = 1.42\text{-}nH \tag{4.7}$$

$$C_1 = \frac{(10.2 - 3.6) \times 10^9}{4\pi \times 3.6 \times 10.1 \times 10^{18} \times 100} = 142.26\text{-}fF \tag{4.8}$$

$$C_2 = \frac{1}{\pi(10.2 - 3.6) \times 10^9 \times 100} = 489.70\text{-}fF \tag{4.9}$$

The T-section filter of figure 4.11a was converted into the balanced version presented in 4.11b. When ideal components are used, both versions have exactly the same frequency response, illustrated in figure 4.12.

The red curve represents the transfer function response of the bandpass filter when the technology models - provided by the foundry - are used. The real components have a varying quality factor depending on the frequency and have a limited bandwidth. These factors explain the small difference in the cut-off frequencies, specially in the 10.1-GHz one. The attenuation in the filter response is caused by the parasitic resistors associated to the inductors and capacitors. The unloaded quality factors of the inductors used are in the range of 18 to 20, therefore not affecting significantly the frequency response of the designed filter.

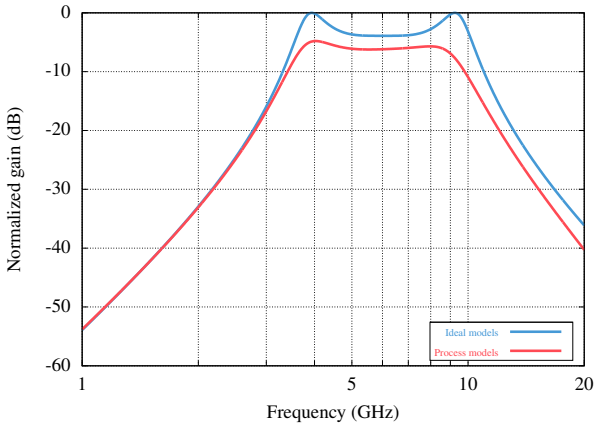

Figure 4.12: Output filter transfer function response.

Figure 4.13a shows the output waveform and 4.13b the respective power spectral density estimation. The first impulse represents a "1" and the second a "0" and therefore they are 180 degrees out of phase.

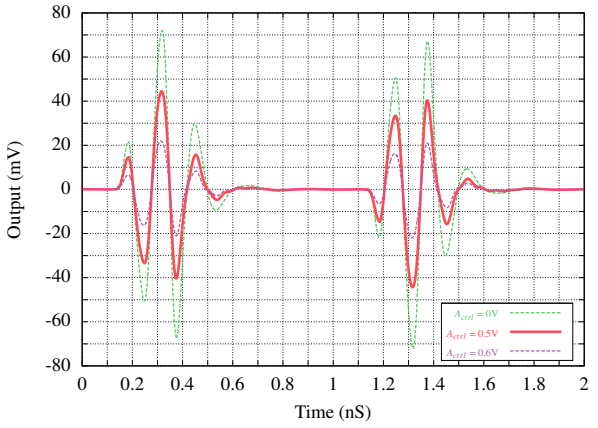

(a) Output waveform

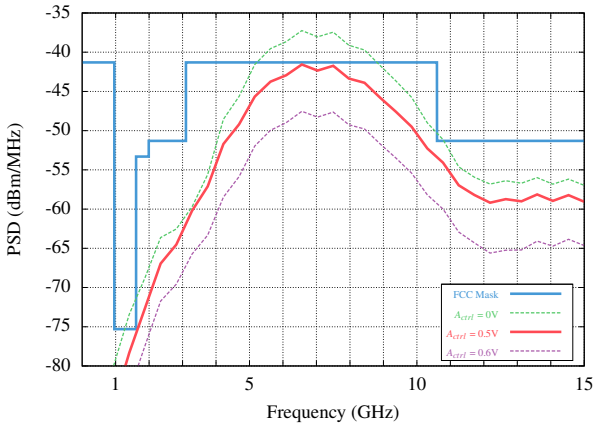

(b) Output waveform PSD

Figure 4.13: Output waveform and its PSD as function of A_{ctrl}.

Three different voltages were applied to A_{ctrl} to demonstrate the output amplifier amplitude tuning. The PSD estimation was obtained using the Cadence Spectre PSD function with a pulse train of 10 impulses, a pulse repetition frequency of 1-GHz and 180 degrees of phase difference between two consecutive pulses.

As observed, the -10-dB bandwidth is approximately 6-GHz and the output PSD respects the FCC mask when $A_{ctrl} \leq 0.5\text{-}V$.

4.3 Physical implementation

Owing the high-frequency of operation, a small technology is mandatory. Most of the bibliography found use 0.18-μm processes. In order to chose a suitable CMOS process, two 90-nm technologies were evaluated [1]:

- **Taiwan Semiconductor Manufacturing Company (TSMC) N90-CMOS-MS-RF-LP** [61]: A 90-nm CMOS process for mixed-signal and radio-frequency applications with low-power consumption.
- **United Microelectronics Corporation (UMC) L90N-MM-RF** [62]: A 90-nm CMOS process for logic, mixed mode and radio-frequency applications with low-κ dielectrics, low leakage and triple-well option.

The selected was the UMC L90N-MM-RF process with triple-well option. Triple-well increases the isolation of both transistors (n and p-channel) from the chip substrate. It also allows circuits to be independent of the substrate bias conditions, which is an advantage for noise isolation, mixed signal and dynamic threshold MOSFET applications [63]. Figure 4.14 depicts a typical triple-well structure.

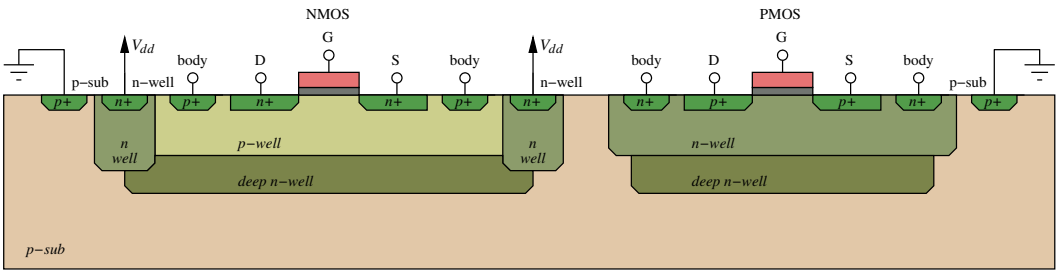

Figure 4.14: Triple-well structure (simplified).

The design rules check (DRC), layout-versus-schematic check (LVS) and the parasitics extraction were made using Mentor Graphics Calibre. There were taken into account practical aspects

[1] The details about the processes comparison cannot be published due to non-disclosure agreements.

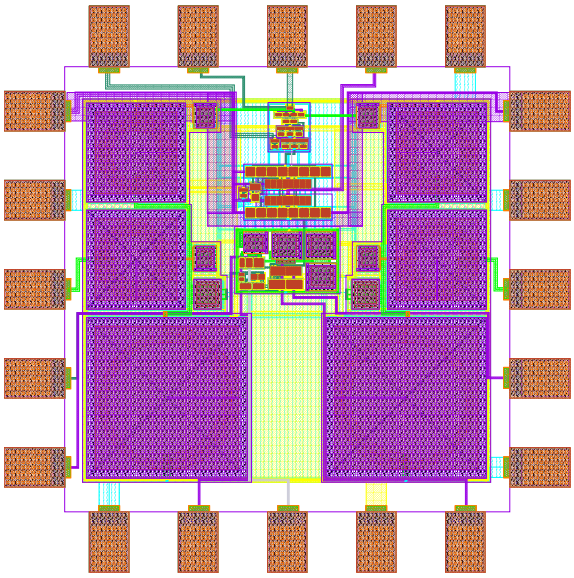

Figure 4.15: Physical implementation (675x675-μm^2).

such as the maximum current densities, connections to the substrate, circuit symmetry amoung others. The physical design is an iterative process where the circuit is improved several times until the final result is reached. The output pad models were also included in the final circuit.

4.4 Results

Before the physical design, all the simulations were done with schematics netlists. These netlists do not have any information about parasitic components such as capacitors and resistances. When the physical design is complete it is possible to extract the circuit parasitic components and obtain a post-layout netlist, which is a much better approximation to the real integrated circuit than the schematic. Once again, Mentor Graphics Calibre was used for this function, specifically the Parasitic Extraction (PEX) tool.

The post-layout netlist was then used for simulation and the results were compared with the schematic netlist. Figure 4.16 shows the output waveform and its power spectral density.

Table 4.2 presents an numerical comparison between pre and post-layout simulations. The values for the tuning circuits were adjusted to meet the FCC mask specification.

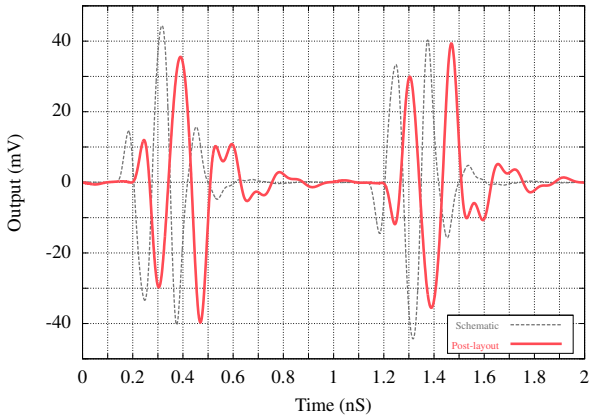

(a) Output waveform

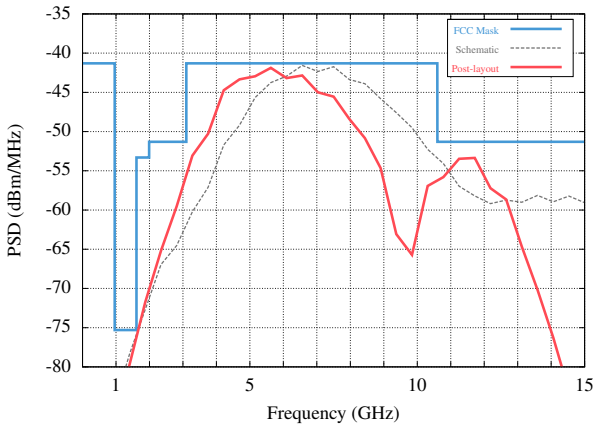

(b) Output power spectral density

Figure 4.16: Schematic versus post-layout results.

	Energy per pulse (pJ)	Pulse amplitude (mV)	Pulse lenght (ps)	Center frequency (GHz)	Bandwidth (GHz)	Peak PSD (dBm/MHz)
Schematic	14.4	83	380	6	7	-41.3
Post-layout	14.6	74	423	5.6	5.4	-42.0

Table 4.2: Schematic versus post-layout results comparison.

From figure 4.16 and table 4.2 it is possible to conclude that the post-layout model complies with the FCC mask and it is identical to the initial schematic model. The main difference between the two cases is the center frequency of the output impulse. This is due to the high impact of the parasitic components in the ring-oscillator output frequency. From the analysis of the raw netlist, it was possible to conclude that the parasitics capacitors are very small (usually a few femto farad). However the connection series resistances are very high and in some cases greater than one ohm. To overcome this, the layout can be further improved by enlarging the metal connection to decrease its resistance.

This work is the second with a smaller energy consumption per impulse and has the greater impulse rate when compared with the literature analyzed as shown in figure 4.17. In addition, has three degrees of freedom for calibration, which make this transmitter very reliable.

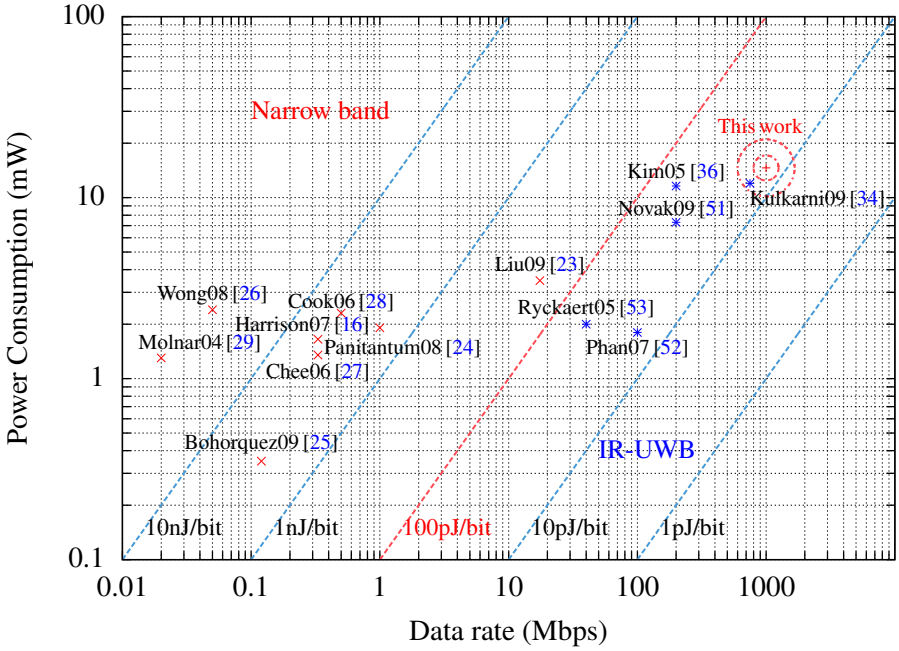

Figure 4.17: Final comparison.

The distribution of the energy consumption per bit is shown in figure 4.18. The output amplifier almost does not consume any energy and the overall energy per pulse is divided between the glitch generator and the ring-oscillator.

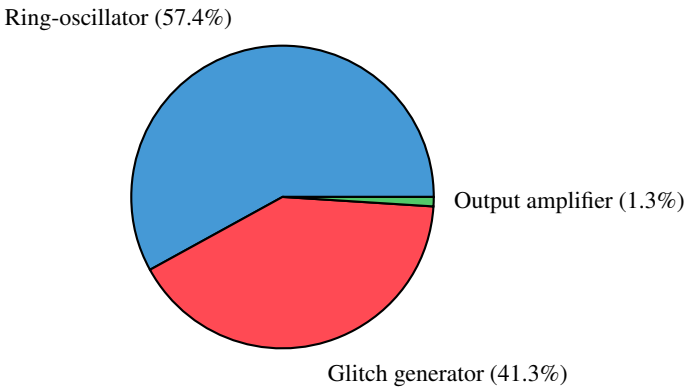

Figure 4.18: Energy consumption distribution percentage per block.

4.4.1 Process corners analysis

A process corner refers to a variation of fabrication parameters of an integrated circuit. These process corners represent the higher deviation from the typical parameters within which a circuit that has been built in silicon must function correctly. A circuit running on devices fabricated at these process corners may run slower or faster than specified and at lower or higher temperatures and voltages, but if the circuit does not function at all at any of these process extremes the design is considered to have inadequate design margin [64].

One naming convention for process corners is to use two-letter designators, where the first letter refers to the NMOS corner, and the second letter refers to the PMOS corner. In this naming convention, three corners exist: typical, fast and slow as shown in figure 4.19. Fast and slow corners exhibit carrier mobilities that are higher and lower than normal, respectively.

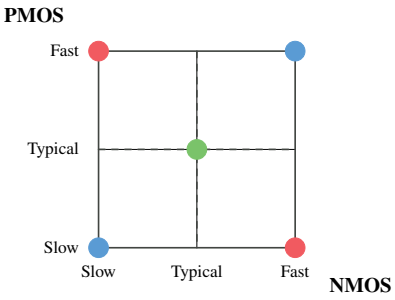

Figure 4.19: CMOS Corners.

There are therefore five possible corners: typical-typical (TT), fast-fast (FF), slow-slow (SS), fast-slow (FS), and slow-fast (SF). The first three corners (TT, FF, SS) marked with green and blue circles are called even corners, because both types of devices are affected evenly, and generally do not adversely affect the logical correctness of the circuit. The resulting devices can function at slower or faster clock frequencies, and are often binned as such. The last two corners (FS, SF) masked with red circles, are called "skewed" corners and usually are a cause for concern. This is because one type will switch much faster than the other, and this form of imbalanced switching can cause one edge of the output to have much less slew than the other edge. In addition to the transistor corners themselves, there are more on-chip variation effects that manifest themselves at smaller technology nodes. These include process, voltage and temperature (PVT) variation effects on on-chip interconnections, as well as via structures.

As indicated in section 4.1 there are three different levels of freedom that allow the tuning of the output pulse after the chip production. In order to test the chip tuning in the worst case conditions, a corner analysis was conducted and the results are illustrated in figures 4.20-4.23.

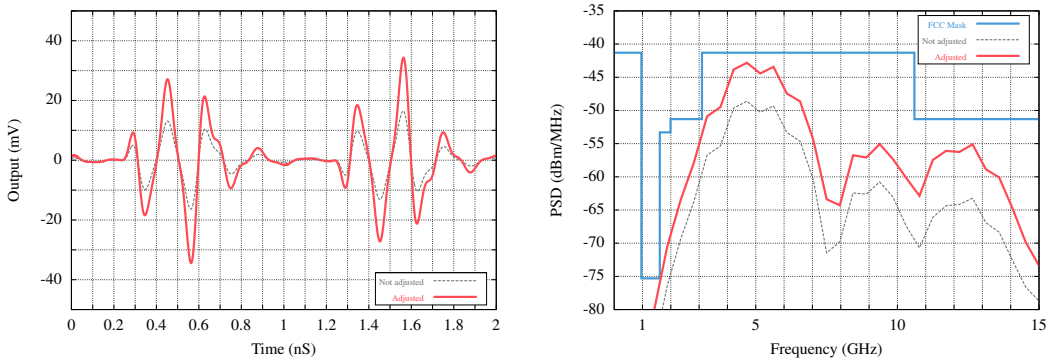

(a) Output waveform **(b)** Output power spectral density

Figure 4.20: Post-layout SS corner results.

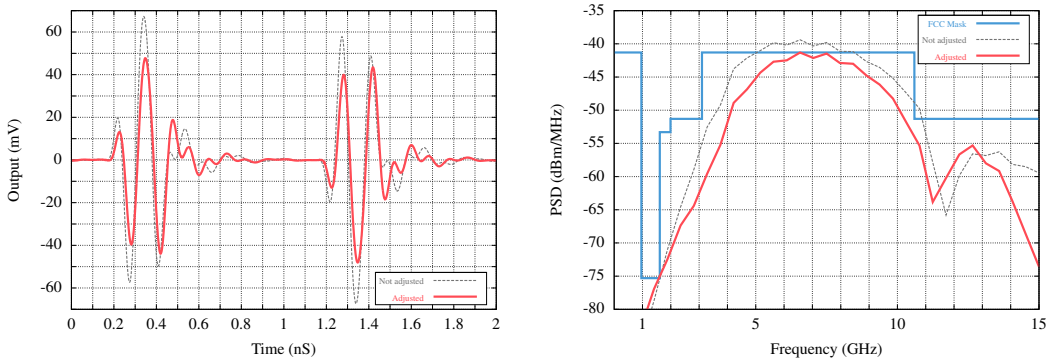

(a) Output waveform **(b)** Output power spectral density

Figure 4.21: Post-layout FF corner results.

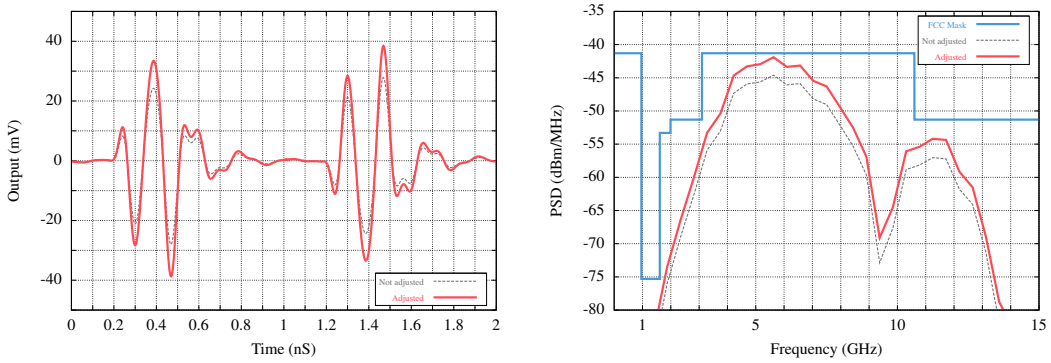

(a) Output waveform **(b)** Output power spectral density

Figure 4.22: Post-layout FS corner results.

It is possible to observe that the worst case scenario is when both N and PMOS are slow 4.20. In this case, the signal center frequency decreases and the bandwidth is severely shortened to 3.9-GHz against the 5.4-GHz of the TT corner. The impulse amplitude is also much smaller but it can

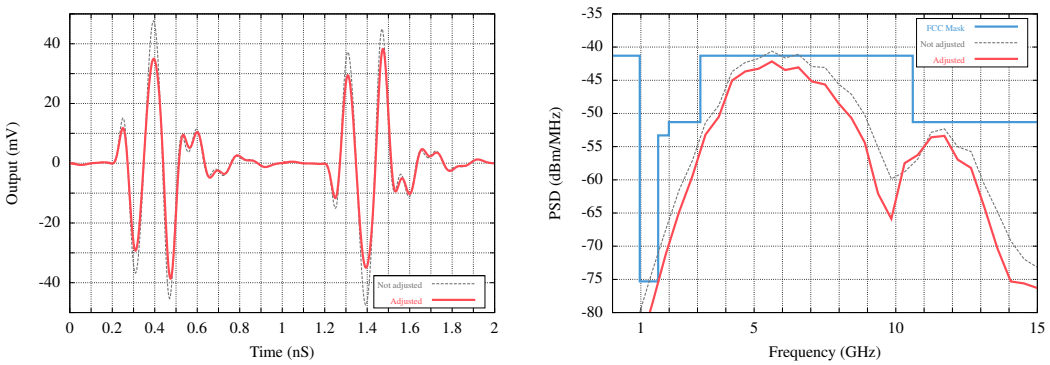

(a) Output waveform

(b) Output power spectral density

Figure 4.23: Post-layout SF corner results.

easily be increased by adjusting the output amplifier gain.

In terms of bandwidth, the FF corner is the most favorable. In this situation the center frequency and the bandwidth increases. This is an expected result, since when both types of transistors are fast, the ring-oscillator will increase its oscillation frequency and the glitch generator will be able to produce shorten glitches, increasing the bandwidth. In this corner, two levels of freedom were used to calibrate the output waveform and comply with the FCC mask: the glitch length was increased, reducing the output signal bandwidth and the output amplifier gain was decreased.

In terms of center frequency and bandwidth, the FS and SF corners are identical. The only difference is that the FS needs an increase of the output amplifier gain unlike the SF corner that needs a decrease. The similar results with FS and SF corners are explained by the fact that the presented solution is fully-differential.

The numerical results of the corner analysis are presented in table 4.3.

It is possible to conclude that even in the worst condition it is easy to calibrate the output shape in order to comply with the FCC UWB mask. The consumption of the impulse generator may vary from 13.3 to 18.9-pJ per impulse for a pulse repetition frequency of 1-GHz.

	Energy per pulse (pJ)	Pulse amplitude (mV)	Pulse lenght (ps)	Center frequency (GHz)	Bandwidth (GHz)	Peak PSD (dBm/MHz)
Typical	14.6	74	423	5.6	5.4	-42.0
FF NA	19.6	123	305	6.6	7.0	-39.4
FF A	18.9	91	383	7.0	6.3	-41.1
SS NA	13.2	29	583	4.9	3.7	-48.8
SS A	13.3	61	596	4.9	3.9	-42.8
FNSP NA	15.6	52	435	5.7	4.8	-44.7
FNSP A	15.7	72	430	5.6	4.9	-42.0
SNFP NA	14.3	91	424	5.9	5.5	-40.6
SNFP A	14.6	72	429	5.6	5.2	-42.1

Table 4.3: Post-layout corner simulations results (NA means not adjusted, A means adjusted).

Chapter 5

Conclusion and future work

The biomedical technology is evolving each day leading to an increase of complexity: brain implants, visual, cochlear, pacemakers, diagnostic equipments, etc. This extra complexity requires higher bit rates to transmit larger amounts of data.

Narrowband wireless systems for very high bit-rates are very difficult to implement, resulting on high hardware complexity. Moreover these systems are based on a carrier frequency, which requires a radio-frequency synthesizer that must be always operating, resulting on constant power consumption. The conventional power amplifiers also have a low efficiency due to high spectral efficiency requirements and the non-constant envelope modulations frequently used.

Recently, with the approval of the UWB unlicensed band by FCC, UWB became an alternative solution to wireless communication with high data-rate capacity, particularly the impulse-radio type. The communication is based on the transmission of narrow pulses (typically smaller than 1-nS) spaced by relatively large amounts of time. This results on very low duty-cycle and low power consumption, since the whole system can be turned off between pulses.

5.1 Achievements

During this thesis, several existing ultra-wideband and narrowband transmitter were studied and compared. An new tunable IR-UWB transmitter for biomedical implants was designed in a 90-nm CMOS process. The transmitter generated bi-phase modulated pulses with a center frequency of 5.6-GHz and a -10-dB bandwidth of 5.4-GHz. The highest pulse repetition rate is 1-Gb/s with an energy consumption of 14.6-pJ/b. The transmitted pulses comply with the FCC spectrum mask and the total circuit area is 675x675-μm^2. The proposed solution allows for the adjustment of the output waveform duration, center frequency and amplitude, in order to comply with the existing regulations as proved by the corner analysis. It also provides a flexible way of UWB transmission using different modulation schemes, namely BPSK, OOK, PPM and PAM.

5.2 Future work

As mentioned in the last section, the objectives of this work were accomplished with success. However, there is always space for improvements. For example, the output filter may be optimized to reduce the number of components and consequently the total circuit area. The ring-oscillator and the glitch generator blocks may also be improved to reduce the power consumption making this transmitter the one with the lowest energy consumption when comparing with the existing implementations.

The simulation results need to be validated in practice and therefore the integrated circuit must be produced and tested to conclude this work. With that goal in mind, the designed integrated circuit is in a way that can be submitted for manufacturing through the Europractice IC service. This will allow practical validation and also a fair comparison with the circuits reported in literature.

The implementation of the proposed solution in an IFN system can be applied directly. In addition, the high data rate provided by the IR-UWB transmitter herein proposed can also open the possibility for multiplexing a high number of neuronal signals. This solution can be a significant advantage over current radio interfaces currently used.

Appendix A

Circuit Schematics

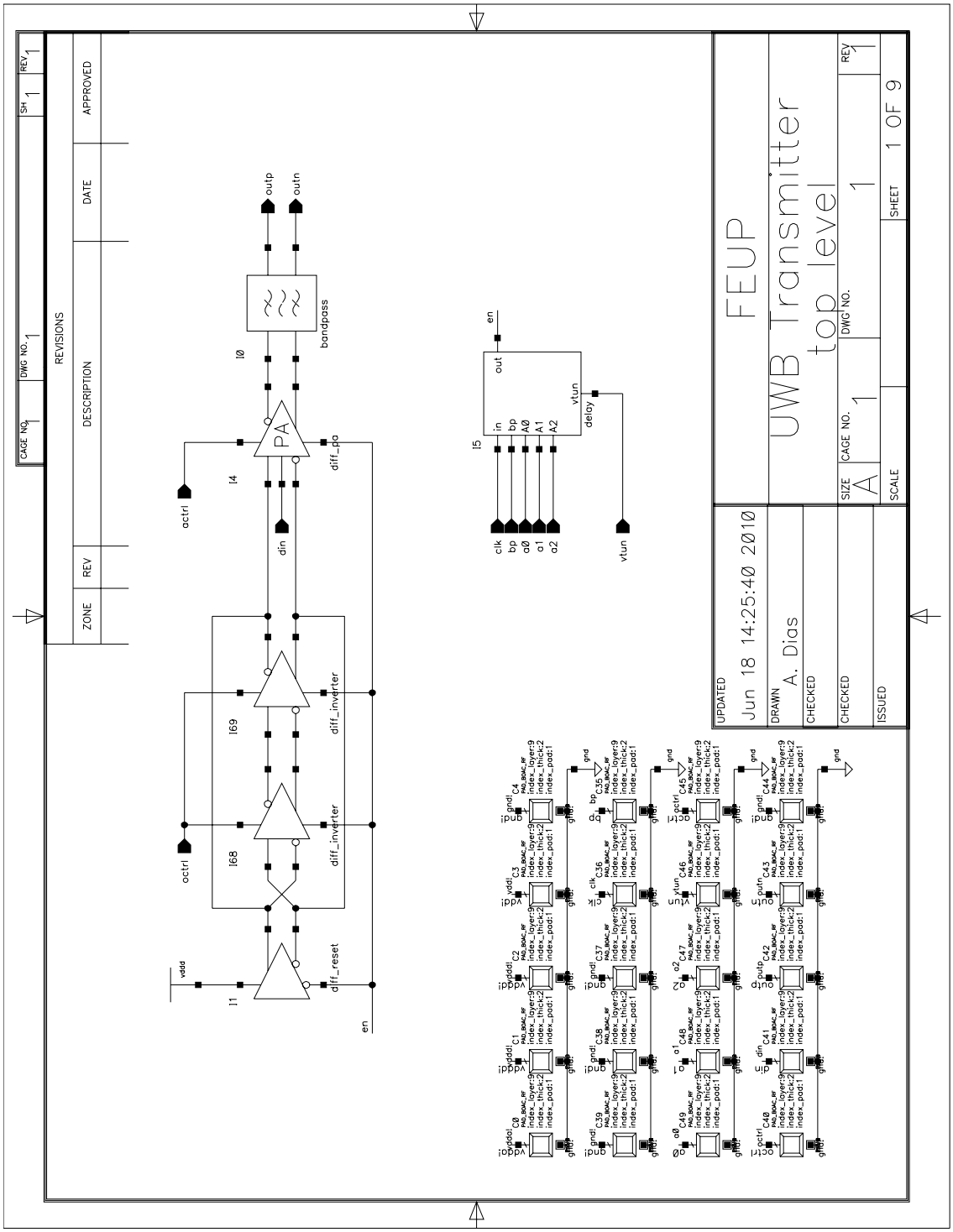

Figure A.1: UWB transmitter top level.

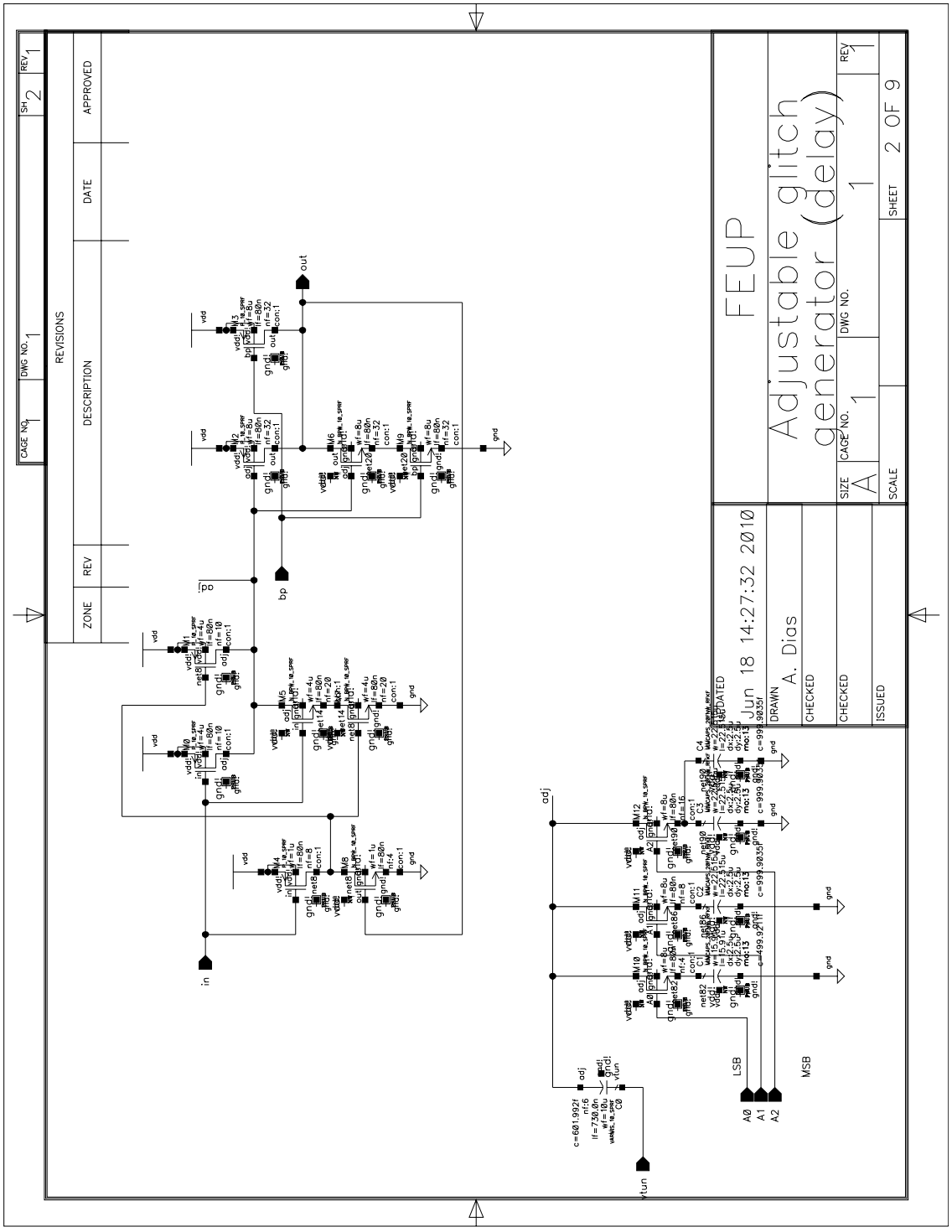

Figure A.2: Adjustable glitch generator complete schematic (delay).

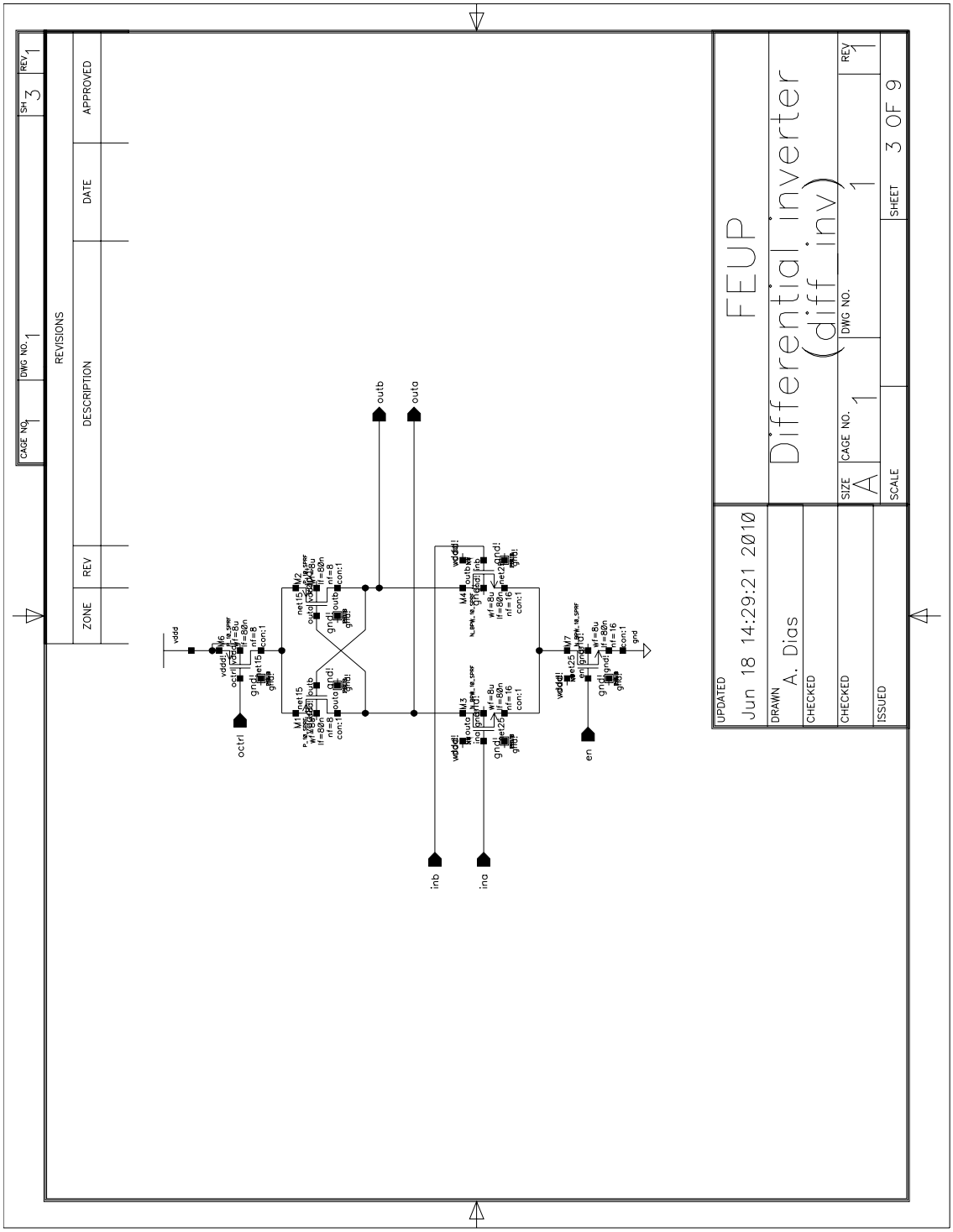

Figure A.3: Differential inverter complete schematic (diff_inv).

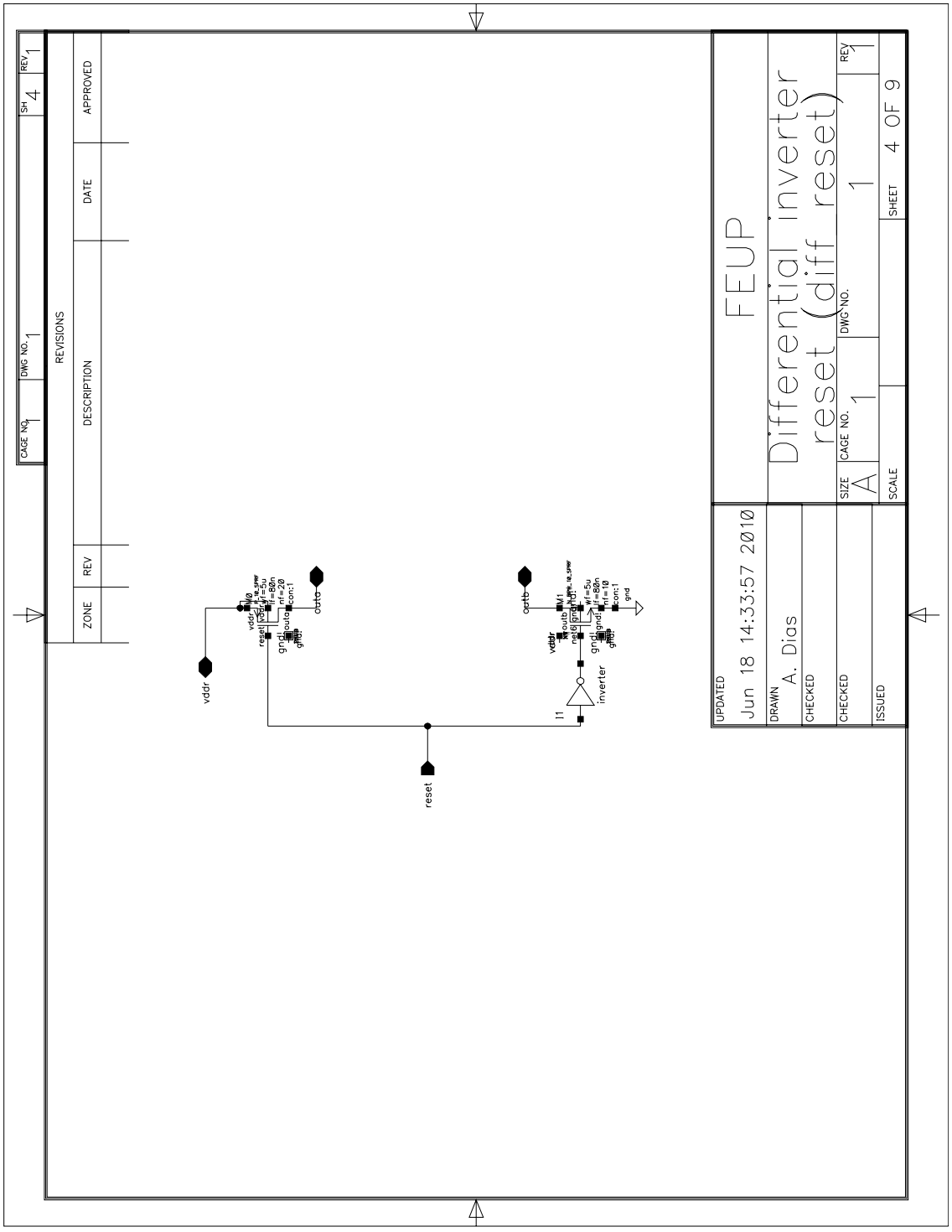

Figure A.4: Differential inverter reset complete schematic (diff_reset).

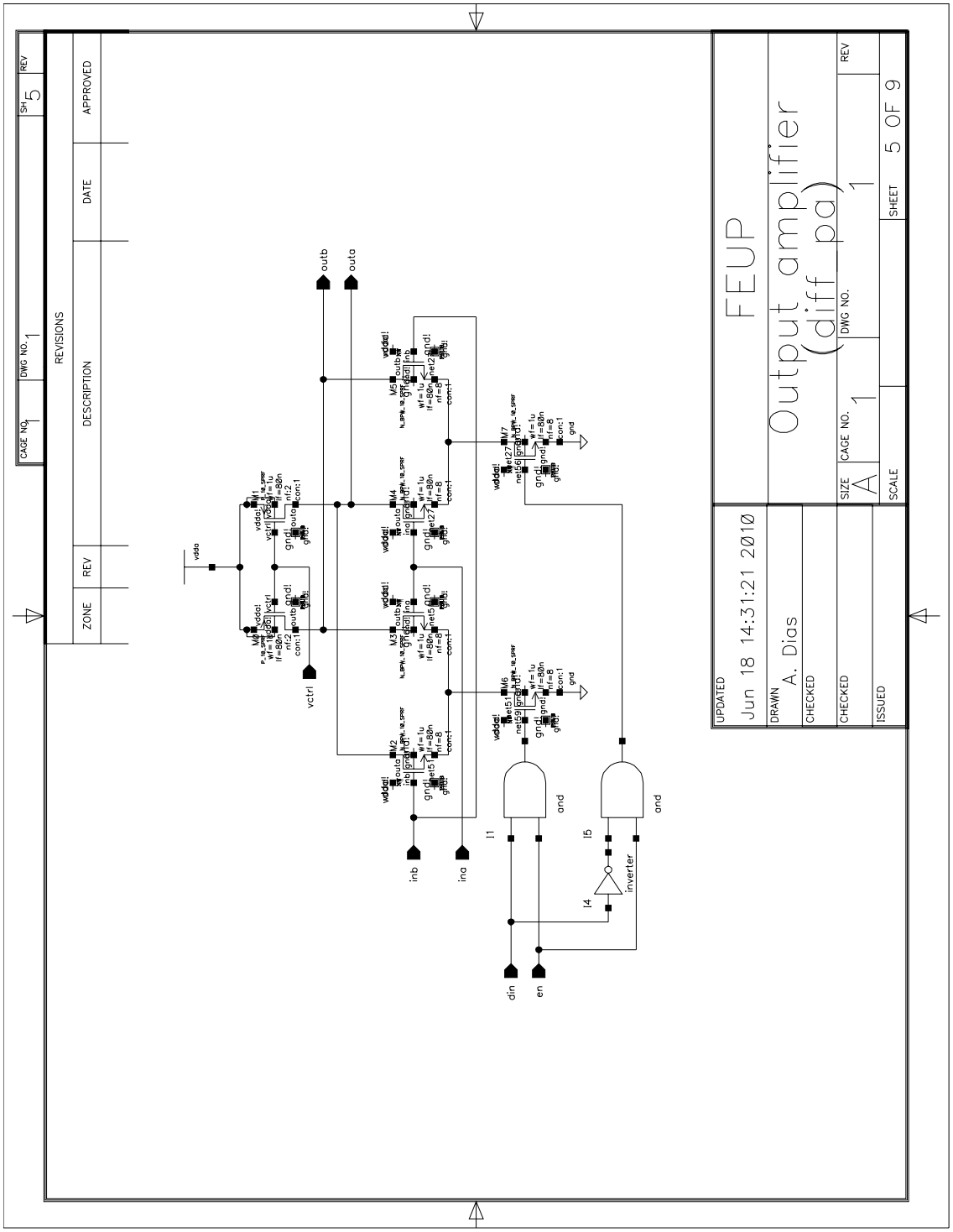

Figure A.5: Output amplifier complete schematic complete schematic (diff_pa).

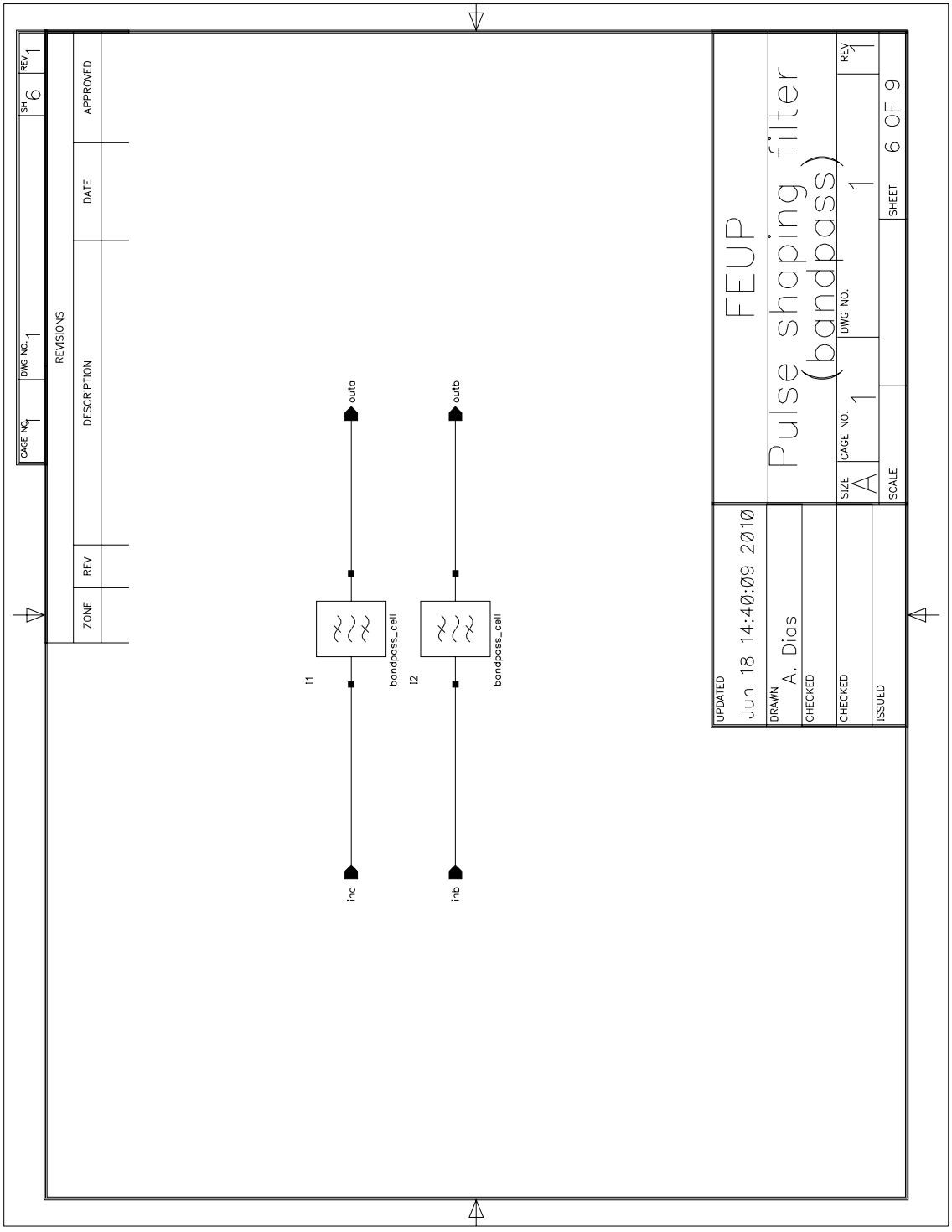

Figure A.6: Differential pulse-shaping filter complete schematic (bandpass).

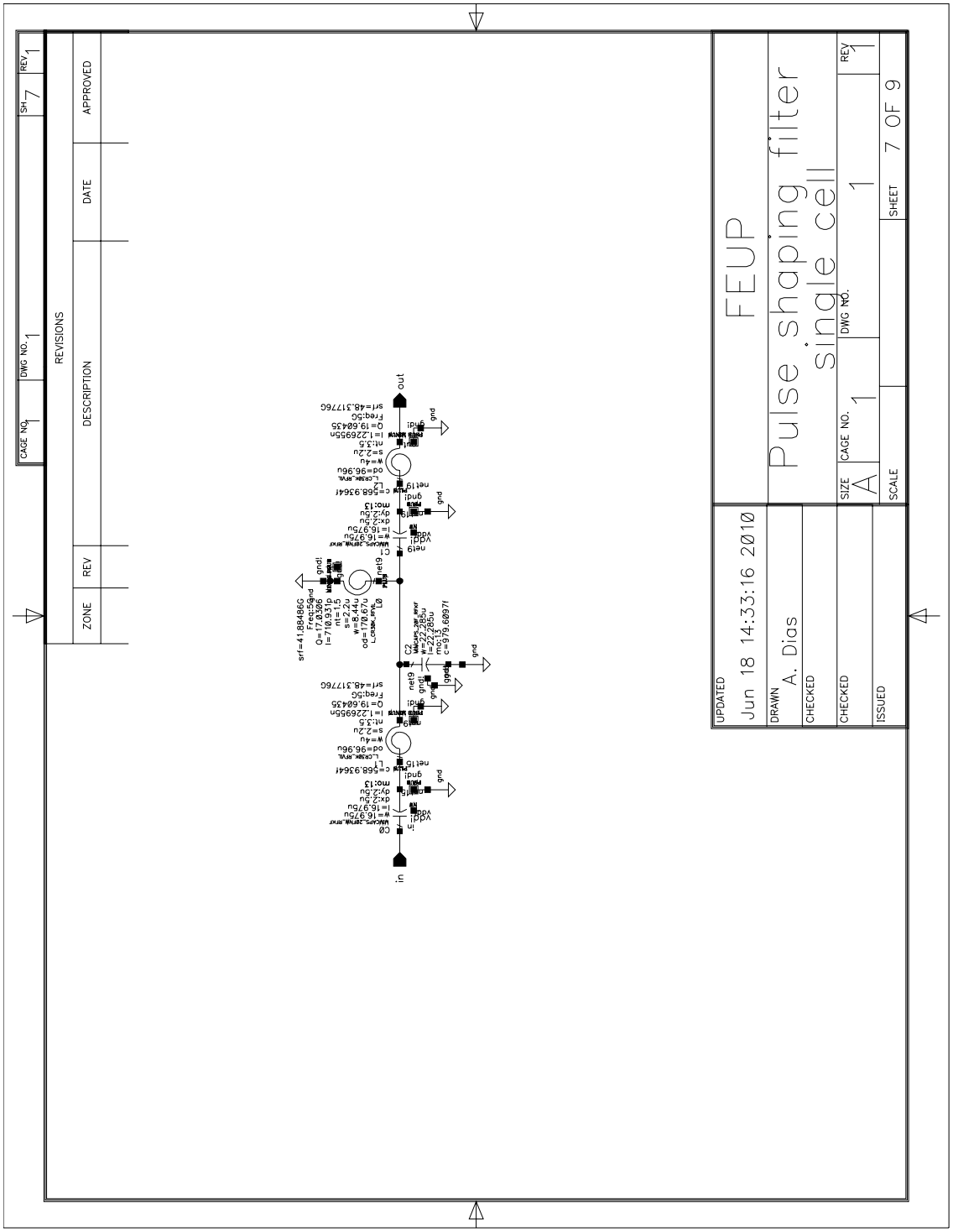

Figure A.7: Pulse-shaping filter single cell complete schematic (bandpass_cell).

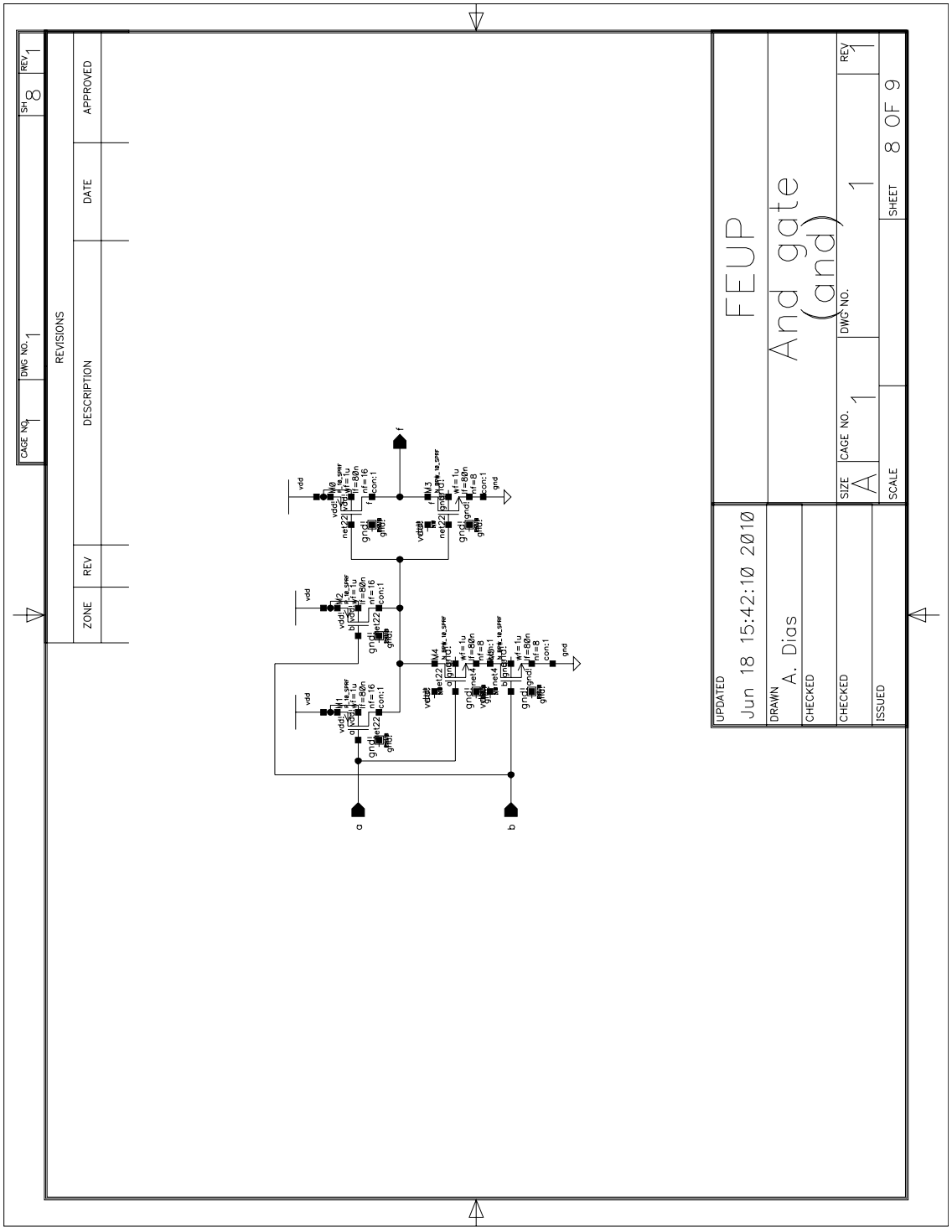

Figure A.8: And gate complete schematic (and).

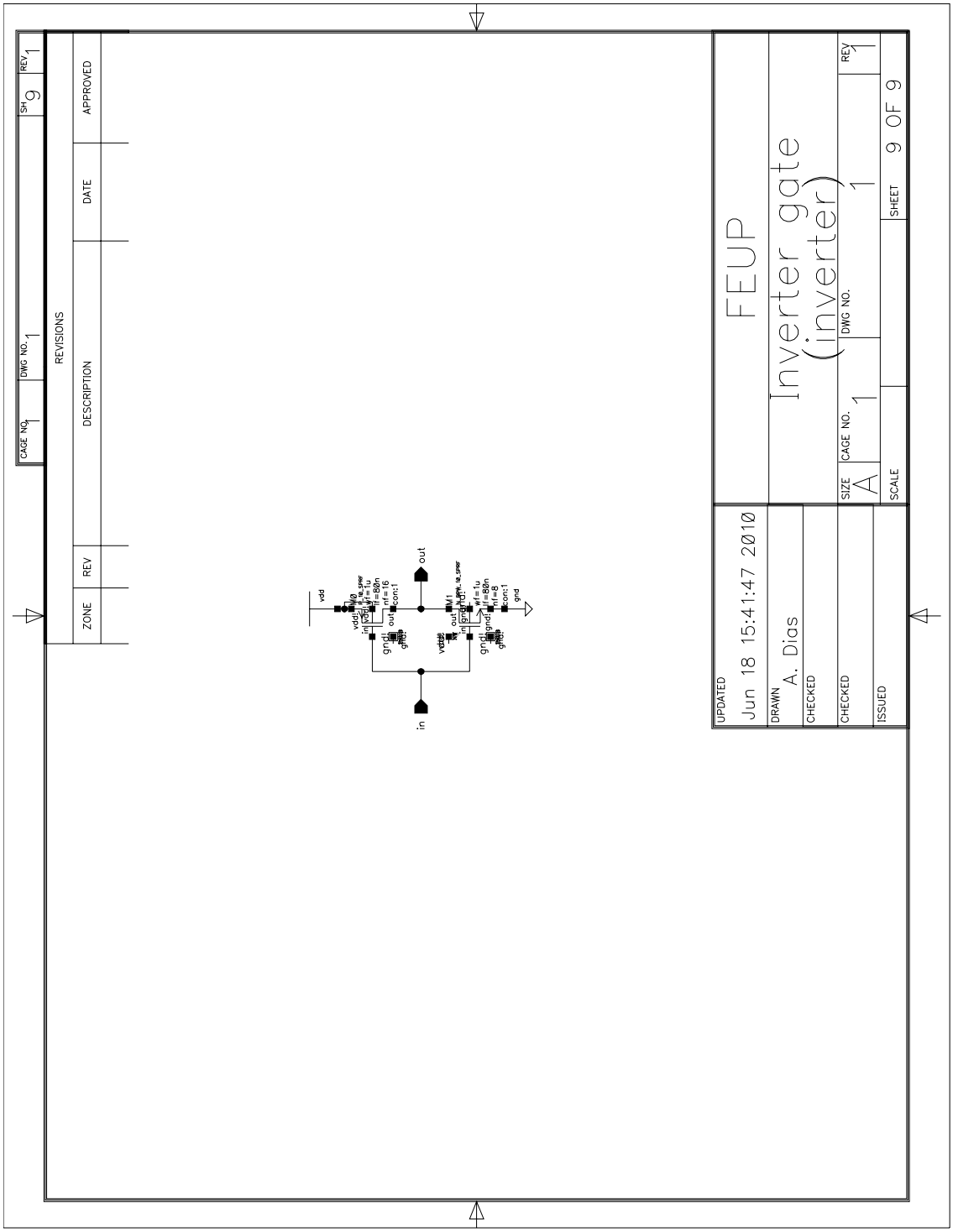

Figure A.9: Inverter gate complete schematic (inv).

Appendix B

Circuit physical implementation

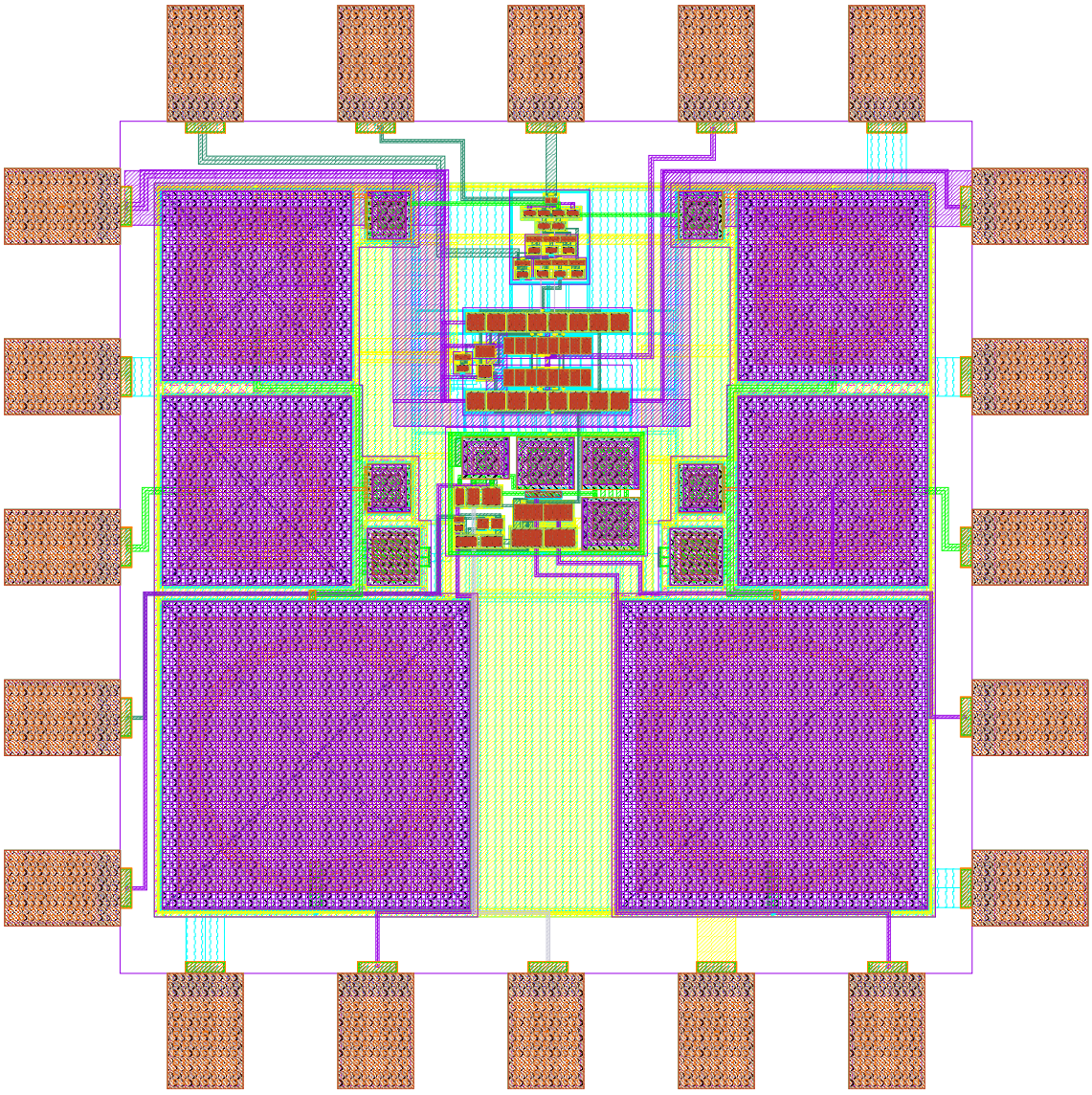

Figure B.1: UWB transmitter physical implementation (675x675-μm^2).

References

[1] J. D. Enderle, J. D. Bronzino, and S. M. Blanchard, *Introduction to biomedical engineering*. Academic Press, April 2005.

[2] B. Franklin, "An account of the effects of electricity in paralytic cases," *Philosophical Transactions of the Royal Society*, vol. 50, pp. 481–482, Jan. 1758.

[3] A. Stanton, "Wilhelm conrad röntgen on a new kind of rays: translation of a paper read before the würzburg physical and medical society, 1895," *Nature*, vol. 53, pp. 274–6, January 1896. [Online]. Available: http://www.nature.com/nature/journal/v53/n1369/pdf/053274b0.pdf

[4] M. Rivera-Ruiz, C. Cajavilca, and J. Varon, "Einthoven's string galvanometer," *Texas Heart Institute Journal*, vol. 35, no. 2, pp. 174–178, March 2008.

[5] The British Medical Journal, "Fifty years of penicillin," *The British Medical Journal*, vol. 1, no. 6171, pp. 1101–1102, Apr. 1979. [Online]. Available: http://www.jstor.org/stable/25432127

[6] H. Berger, "Über das elektrenkephalogramm des menschen," *Archiv für Psychiatrie und Nervenkrankheiten*, vol. 87, no. 1, pp. 527–570, April 1929. [Online]. Available: http://www.scopus.com/inward/record.url?eid=2-s2.0-34250548621&partnerID=40

[7] C. Plummer, A. S. Harvey, and M. Cook, "EEG source localization in focal epilepsy: Where are we now?" *Epilepsia*, vol. 49, no. 2, pp. 201–218, October 2008. [Online]. Available: http://dx.doi.org/10.1111/j.1528-1167.2007.01381.x

[8] L. R. Hochberg, M. D. Serruya, G. M. Friehs, J. A. Mukand, M. Saleh, A. H. Caplan, A. Branner, D. Chen, R. D. Penn, and J. P. Donoghue, "Neuronal ensemble control of prosthetic devices by a human with tetraplegia," *Nature*, vol. 442, no. 7099, pp. 164–171, Jul. 2006. [Online]. Available: http://dx.doi.org/10.1038/nature04970

[9] K. Iniewski, *VLSI Circuits for Biomedical Applications*, 1st ed. Artech House Publishers, Jun. 2008.

[10] Organization for Economic Co-Operation and Development. (2009, December) OECD health data 2009 - frequently requested data. [Online]. Available: http://www.oecd.org/document/16/0,3343,en_2649_34631_2085200_1_1_1_1,00.html

[11] U.S. Department of Commerce, Bureau Of Economic Analysis. (2009, December) National economic accounts. [Online]. Available: http://www.bea.gov/national/index.htm#gdp

[12] St. Jude Medical Inc. (2009, December) Accent DR RF PM2210 Datasheet. [Online]. Available: http://www.sjmprofessional.com/Products/US/Pacing-Systems/Accent-Pacemaker.aspx

[13] Reuters. (2009, December) First Wi-Fi pacemaker in U.S. gives patient freedom. [Online]. Available: http://www.reuters.com/article/idUSTRE5790AK20090811

[14] J. Wessberg, C. R. Stambaugh, J. D. Kralik, P. D. Beck, M. Laubach, J. K. Chapin, J. Kim, S. J. Biggs, M. A. Srinivasan, and M. A. L. Nicolelis, "Real-time prediction of hand trajectory by ensembles of cortical neurons in primates," *Nature*, vol. 408, no. 6810, pp. 361–365, Nov. 2000. [Online]. Available: http://dx.doi.org/10.1038/35042582

[15] M. D. Serruya, N. G. Hatsopoulos, L. Paninski, M. R. Fellows, and J. P. Donoghue, "Instant neural control of a movement signal," *Nature*, vol. 416, no. 6877, pp. 141–142, Mar. 2002, PMID: 11894084. [Online]. Available: http://www.ncbi.nlm.nih.gov/pubmed/11894084

[16] R. R. Harrison, P. T. Watkins, R. J. Kier, R. O. Lovejoy, D. J. Black, B. Greger, and F. Solzbacher, "A low-power integrated circuit for a wireless 100-electrode neural recording system," *IEEE Journal of Solid-State Circuits*, vol. 42, no. 1, pp. 123–133, Jan. 2007.

[17] R. Bashirullah, J. Harris, J. Sanchez, T. Nishida, and J. Principe, "Florida wireless implantable recording electrodes (FWIRE) for brain machine interfaces," in *IEEE International Symposium on Circuits and Systems*, May 2007, pp. 2084–2087.

[18] FCC, "Mics band plan, part 95," January 2003.

[19] H. Savci, A. Sula, Z. Wang, N. Dogan, and E. Arvas, "MICS transceivers: regulatory standards and applications medical implant communications service," in *IEEE SoutheastCon*, April 2005, pp. 179–182. [Online]. Available: http://dx.doi.org/10.1109/SECON.2005.1423241

[20] FCC, "WMTS band plan, part 95," March 2003.

[21] B. Otis, Y. Chee, and J. Rabaey, "A 400 μW-RX, 1.6mW-TX super-regenerative transceiver for wireless sensor networks," in *IEEE International Solid-State Circuits Conference*, vol. 1, Feb. 2005, pp. 396–606. [Online]. Available: http://dx.doi.org/10.1109/ISSCC.2005.1494036

[22] A. Sodagar, G. Perlin, Y. Yao, K. Najafi, and K. Wise, "An implantable 64-channel wireless microsystem for single-unit neural recording," *IEEE Journal of Solid-State Circuits*, vol. 44, no. 9, pp. 2591–2604, September 2009. [Online]. Available: http://dx.doi.org/10.1109/JSSC.2009.2023159

[23] Y.-H. Liu, C.-L. Li, and T.-H. Lin, "A 200-pJ/b MUX-Based RF transmitter for implantable multichannel neural recording," *IEEE Transactions on Microwave Theory and Techniques*, vol. 57, no. 10, pp. 2533–2541, Oct. 2009. [Online]. Available: http://dx.doi.org/10.1109/TMTT.2009.2029955

[24] N. Panitantum, K. Mayaram, and T. Fiez, "A 900-MHz low-power transmitter with fast frequency calibration for wireless sensor networks," in *IEEE Custom Integrated Circuits Conference*, Sept. 2008, pp. 595–598. [Online]. Available: http://dx.doi.org/10.1109/CICC.2008.4672156

[25] J. Bohorquez, A. Chandrakasan, and J. Dawson, "A 350 μW CMOS MSK transmitter and 400 μW OOK super-regenerative receiver for medical implant communications," *IEEE Journal of Solid-State Circuits*, vol. 44, no. 4, pp. 1248–1259, April 2009. [Online]. Available: http://dx.doi.org/10.1109/JSSC.2009.2014728

[26] A.-W. Wong, D. McDonagh, G. Kathiresan, O. Omeni, O. El-Jamaly, T.-K. Chan, P. Paddan, and A. Burdett, "A 1v, micropower system-on-chip for vital-sign monitoring in wireless body sensor networks," in *Digest of Technical Papers. IEEE International Solid-State Circuits Conference*, Feb. 2008, pp. 138–602. [Online]. Available: http://dx.doi.org/10.1109/ISSCC.2008.4523095

[27] Y. Chee, A. Niknejad, and J. Rabaey, "A 46% efficient 0.8dBm transmitter for wireless sensor networks," in *Symposium on VLSI Circuits*, 0-0 2006, pp. 43–44. [Online]. Available: http://dx.doi.org/10.1109/VLSIC.2006.1705303

[28] B. Cook, A. Berny, A. Molnar, S. Lanzisera, and K. Pister, "An ultra-low power 2.4GHz RF transceiver for wireless sensor networks in 0.13/spl mu/m CMOS with 400mV supply and an integrated passive RX front-end," in *Digest of Technical Papers. IEEE International Solid-State Circuits Conference*, Feb. 2006, pp. 1460–1469. [Online]. Available: http://dx.doi.org/10.1109/ISSCC.2006.1696196

[29] A. Molnar, B. Lu, S. Lanzisera, B. Cook, and K. Pister, "An ultra-low power 900 MHz RF transceiver for wireless sensor networks," in *Proceedings of the IEEE Custom Integrated Circuits Conference*, Oct. 2004, pp. 401–404. [Online]. Available: http://ieeexplore.ieee.org/stamp/stamp.jsp?tp=&arnumber=1652904&isnumber=34642&type=ref

[30] FCC. (2002, February) Revision of part 15 of the commission's rules regarding ultra-wideband transmission systems. [Online]. Available: http://hraunfoss.fcc.gov/edocs_public/attachmatch/FCC-02-48A1.pdf

[31] X. Shen, M. Guizani, R. C. Qiu, and T. Le-Ngoc, *Ultra-Wideband Wireless Communications and Networks*, 1st ed. Wiley, Apr. 2006.

[32] O. Novak, W. Wu, and C. Charles, "Wireless ultra-wideband data link for biomedical implants," Ph.D. dissertation, July 2009.

[33] S. Lida, K. Tanaka, H. Suzuki, N. Yoshikawa, N. Shoji, B. Griffiths, D. Mellor, F. Hayden, I. Butler, and J. Chatwin, "A 3.1 to 5 GHz CMOS DSSS UWB transceiver for WPANs," in *IEEE International Solid-State Circuits Conference*, vol. 1, Feb. 2005, pp. 214–594. [Online]. Available: http://dx.doi.org/10.1109/ISSCC.2005.1493945

[34] V. Kulkarni, M. Muqsith, K. Niitsu, H. Ishikuro, and T. Kuroda, "A 750 Mb/s, 12 pJ/b, 6-to-10 GHz CMOS IR-UWB transmitter with embedded on-chip antenna," *IEEE Journal of Solid-State Circuits*, vol. 44, no. 2, pp. 394–403, Feb. 2009.

[35] S. Sim, D.-W. Kim, and S. Hong, "A CMOS UWB pulse generator for 6–10 GHz applications," *IEEE Microwave and Wireless Components Letters*, vol. 19, no. 2, pp. 83–85, Feb. 2009. [Online]. Available: http://dx.doi.org/10.1109/LMWC.2008.2011318

[36] H. Kim and Y. Joo, "Fifth-derivative Gaussian pulse generator for UWB system," in *IEEE Radio Frequency integrated Circuits (RFIC) Symposium*, June 2005, pp. 671–674. [Online]. Available: http://dx.doi.org/10.1109/RFIC.2005.1489903

[37] L. Michael, M. Ghavami, and R. Kohno, "Multiple pulse generator for ultra-wideband communication using hermite polynomial based orthogonal pulses," in *IEEE Conference on Ultra Wideband Systems and Technologies*, 2002, pp. 47–51. [Online]. Available: 10.1109/UWBST.2002.1006316

[38] H. Sheng, P. Orlik, A. Haimovich, J. Cimini, L.J., and J. Zhang, "On the spectral and power requirements for ultra-wideband transmission," in *IEEE International Conference on Communications*, vol. 1, May 2003, pp. 738–742. [Online]. Available: http://ieeexplore.ieee.org/xpls/abs_all.jsp?arnumber=1204271

[39] X. Chen and S. Kiaei, "Monocycle shapes for ultra wideband system," in *IEEE International Symposium on Circuits and Systems*, vol. 1, May 2002, pp. 597–600. [Online]. Available: http://dx.doi.org/10.1109/ISCAS.2002.1009911

[40] S. M. Salahuddin, S. Raju, S. Islam, and P. K. Saha, "DSSS-IR-UWB transceiver for intra/inter chip wireless interconnection in future ULSI," in *International Conference on Electrical and Computer Engineering*, 19-21 2006, pp. 108–111.

[41] W. Vereecken and M. Steyaert, *Ultra-Wideband Pulse-based Radio: Reliable Communication Over a Wideband Channel*. Springer, May 2009.

[42] S. Kandeepan, G. Baldini, and R. Piesiewicz, "Preliminary experimental results on the spectrum sensing performances for UWB-cognitive radios for detecting IEEE 802.11n systems," in *International Symposium on Wireless Communication Systems*, October 2009, pp. 111–115.

[43] K. Siwiak and D. McKeown, *Ultra-wideband radio technology*. John Wiley and Sons, 2004.

[44] T. Aytur, H.-C. Kang, R. Mahadevappa, M. Altintas, S. Brink, T. Diep, C.-C. Hsu, F. Shi, F.-R. Yang, C.-C. Lee, R.-H. Yan, and B. Razavi, "A fully integrated UWB PHY in 0.13/spl mu/m CMOS," in *Digest of Technical Papers. IEEE International Solid-State Circuits Conference*, Feb. 2006, pp. 418–427.

[45] M. Win and R. Scholtz, "Impulse radio: how it works," *IEEE Communications Letters*, vol. 2, no. 2, pp. 36–38, 1998. [Online]. Available: 10.1109/4234.660796

[46] F. Ramirez-Mireles, "On the performance of ultra-wide-band signals in gaussian noise and dense multipath," *Vehicular Technology, IEEE Transactions on*, vol. 50, no. 1, pp. 244–249, Jan 2001. [Online]. Available: http://dx.doi.org/10.1109/25.917932

[47] ——, "Signal design for ultra-wide-band communications in dense multipath," *IEEE Transactions on Vehicular Technology*, vol. 51, no. 6, pp. 1517–1521, Nov 2002. [Online]. Available: http://dx.doi.org/10.1109/TVT.2002.804838

[48] R. Qiu, "A study of the ultra-wideband wireless propagation channel and optimum uwb receiver design," *IEEE Journal on Selected Areas in Communications*, vol. 20, no. 9, pp. 1628–1637, Dec. 2002. [Online]. Available: http://dx.doi.org/10.1109/JSAC.2002.805249

[49] R. Qiu, H. Liu, and X. Shen, "Ultra-wideband for multiple access communications," *IEEE Communications Magazine*, vol. 43, no. 2, pp. 80–87, Feb. 2005. [Online]. Available: http://dx.doi.org/10.1109/MCOM.2005.1391505

[50] D. Barras, F. Ellinger, and H. J\äckel, "A comparison between ultrawideband and narrowband transceivers," *IEEE/TRLabs Wireless*, July 2002.

[51] O. Novak and C. Charles, "Low-power UWB pulse generators for biomedical implants," in *IEEE International Conference on Ultra-Wideband*, September 2009, pp. 778–782. [Online]. Available: http://dx.doi.org/10.1109/ICUWB.2009.5288810

[52] T.-A. Phan, J. Lee, V. Krizhanovskii, S.-K. Han, and S.-G. Lee, "A 18-pJ/Pulse OOK CMOS transmitter for multiband UWB impulse radio," *IEEE Microwave and Wireless Components Letters*, vol. 17, no. 9, pp. 688–690, Sept. 2007.

[53] J. Ryckaert, C. Desset, A. Fort, M. Badaroglu, V. De Heyn, P. Wambacq, G. Van der Plas, S. Donnay, B. Van Poucke, and B. Gyselinckx, "Ultra-wide-band transmitter for low-power wireless body area networks: design and evaluation," *IEEE Transactions on Circuits and Systems I: Regular Papers*, vol. 52, no. 12, pp. 2515–2525, Dec. 2005. [Online]. Available: http://dx.doi.org/10.1109/TCSI.2005.858187

[54] Y. Zheng, H. Dong, and Y. P. Xu, "A novel CMOS/BiCMOS UWB pulse generator and modulator," in *IEEE MTT-S International Microwave Symposium Digest*, vol. 2, 6-11 2004, pp. 1269–1272.

[55] Y. Zheng, Y. Zhang, and Y. Tong, "A novel wireless interconnect technology using impulse radio for interchip communications," *IEEE Transactions on Microwave Theory and Techniques*, vol. 54, no. 4, pp. 1912–1920, june 2006.

[56] J. Rabaey, A. Chandrakasan, and B. Nikolic, *Digital integrated circuits: a design perspective*, 2nd ed. Pearson Education, 2003.

[57] O. Lemaire and T. Xia, "Design of a monolithic width programmable Gaussian monocycle pulse generator for ultra wideband radar in cmos technology," in *Joint IEEE North-East Workshop on Circuits and Systems and TAISA Conference*, june 2009, pp. 1–4.

[58] J. A. McNeill and D. Ricketts, *The Designer's Guide to Jitter in Ring Oscillators*, 1st ed. Springer, Apr. 2009.

[59] S. Park, Y. Choi, S.-G. Lee, Y.-J. Jung, S.-C. Park, and W. Kim, "Low-jitter phase-locked loop based on pseudo-differential delay elements," *Electronics Letters*, vol. 37, no. 11, pp. 669–670, 24 2001.

[60] M. Arshad, *Network Analysis and Synthesis*. Firewall Media, Jun. 2006.

[61] Europractice IC. (2010, June) TSMC 90-nm technology overview. [Online]. Available: http://www.europractice-ic.com/technologies_TSMC.php?tech_id=90nm

[62] ——. (2010, June) UMC 90-nm technology overview. [Online]. Available: http://www.europractice-ic.com/technologies_UMC.php?tech_id=90nm

[63] S. H. Voldman, *ESD: physics and devices*. John Wiley and Sons, Nov. 2004.

[64] N. Weste and D. Harris, *CMOS VLSI Design: A Circuits and Systems Perspective*. Addison-Wesley, Mar. 2010.